Redox Biology 72 (2024) 103156

Contents lists available at ScienceDirect

Redox Biology

journal homepage: www.elsevier.com/locate/redox

Atox1 protects hippocampal neurons after traumatic brain injury via DJ-1 mediated anti-oxidative stress and mitophagy

Pengzhan Zhao [a,1], Wenqian Shi [a,1], Yangfan Ye [a,1], Ke Xu [a], Jingming Hu [a], Honglu Chao [a], ZeQiang Tao [a], Lei Xu [a], Wei Gu [a], Liuchao Zhang [a], Tian Wang [a], Xinyue Wang [a], Jing Ji [a,b,c,*]

[a] Department of Neurosurgery, The First Affiliated Hospital of Nanjing Medical University, Nanjing, China
[b] Gusu School, Nanjing Medical University, Suzhou, China
[c] Department of Neurosurgery, The Affiliated Kizilsu Kirghiz Autonomous Prefecture People's Hospital of Nanjing Medical University, Artux, Xinjiang, China

ARTICLE INFO

Keywords:
Traumatic brain injury
Hippocampal neuron
Atox1
DJ-1
Oxidative stress

ABSTRACT

Regulation of the oxidative stress response is crucial for the management and prognosis of traumatic brain injury (TBI). The copper chaperone Antioxidant 1 (Atox1) plays a crucial role in regulating intracellular copper ion balance and impacting the antioxidant capacity of mitochondria, as well as the oxidative stress state of cells. However, it remains unknown whether Atox1 is involved in modulating oxidative stress following TBI. Here, we investigated the regulatory role of Atox1 in oxidative stress on neurons both in vivo and in vitro, and elucidated the underlying mechanism through culturing hippocampal HT-22 cells with Atox1 mutation. The expression of Atox1 was significantly diminished following TBI, while mice with overexpressed Atox1 exhibited a more preserved hippocampal structure and reduced levels of oxidative stress post-TBI. Furthermore, the mice displayed notable impairments in learning and memory functions after TBI, which were ameliorated by the overexpression of Atox1. In the stretch injury model of HT-22 cells, overexpression of Atox1 mitigated oxidative stress by preserving the normal morphology and network connectivity of mitochondria, as well as facilitating the elimination of damaged mitochondria. Mechanistically, co-immunoprecipitation and mass spectrometry revealed the binding of Atox1 to DJ-1. Knockdown of DJ-1 in HT-22 cells significantly impaired the antioxidant capacity of Atox1. Mutations in the copper-binding motif or sequestration of free copper led to a substantial decrease in the interaction between Atox1 and DJ-1, with overexpression of DJ-1 failing to restore the antioxidant capacity of Atox1 mutants. The findings suggest that DJ-1 mediates the ability of Atox1 to withstand oxidative stress. And targeting Atox1 could be a potential therapeutic approach for addressing post-traumatic neurological dysfunction.

1. Introduction

Traumatic brain injury (TBI) is a disease in which the structure and function of the brain are damaged by external force [1,2]. It can lead to severe short- and long-term neurological disorders that can have a significant impact on a patient's life and quality of life [3–5]. Despite the advances in early intervention and comprehensive rehabilitation measures to improve the prognosis of patients with traumatic craniocerebral injury, specific treatments for traumatic craniocerebral injury and effective treatment at different stages of injury currently remain a challenge [6–8]. Future research needs to further investigate the mechanism of injury, develop individualized treatment strategies, and explore new interventions and rehabilitation tools to improve the prognosis and quality of life of patients.

Abnormal mitochondrial function is a significant contributor to neuronal death [9,10]. Mitochondria serve as the primary site for cellular energy production and play crucial roles in regulating essential processes such as apoptosis, oxidative stress, and calcium homeostasis [11,12]. Impaired mitochondrial function results in diminished energy generation, heightened oxidative stress levels, activation of apoptotic signaling pathways, and disrupted calcium ion balance [12]. Ultimately, these disturbances may culminate in neuronal demise. Copper ions, as

* Corresponding author. Department of Neurosurgery, the First Affiliated Hospital of Nanjing Medical University, 300 Guangzhou Road, Nanjing, Jiangsu, 210029, China.
E-mail address: jijing@njmu.edu.cn (J. Ji).
[1] These authors contributed equally to this work.

https://doi.org/10.1016/j.redox.2024.103156
Received 20 September 2023; Received in revised form 6 April 2024; Accepted 10 April 2024
Available online 12 April 2024

indispensable trace elements in the human body, play a pivotal role in regulating redox reactions and interacting with biological macromolecules within cells [13–15]. Multiple studies have demonstrated that the interplay between copper ions and mitochondrial oxidative stress encompasses various aspects. First, copper ions can modulate the process of oxygen radical production and scavenging by interacting with enzymes in mitochondria, such as copper-zinc superoxide dismutase, thereby influencing the catalytic activity of the enzymes [16–18]. Second, copper ions are also involved in the regulation of mitochondrial membrane potential [19]. The copper transport proteins ATP7A and ATP7B located in the endoplasmic reticulum are believed to participate in regulating mitochondrial membrane potential, which subsequently affects mitochondrial function and cell survival. In addition, some research has indicated that free copper ions have redox activity and are capable of generating reactive oxygen species and are therefore potentially toxic to cells [20,21]. Overall, the relationship between copper ions and mitochondrial oxidative stress is intricate and further exploration of copper ions and copper proteins is needed to fully understand the mechanisms of cellular oxidative stress and related central nervous system diseases.

Copper proteins are a group of proteins that bind copper ions, including copper transport proteins that regulate the concentration and location of copper ions in the cell, and that handle the uptake and export of copper, as well as the selective delivery of copper to copper-dependent enzymes [22–25]. Upon the uptake of copper ions by the transmembrane Ctr1 trimer [26–28], the small copper chaperone molecule Atox1 transports the metal to two multidomain P_{1B}-type ATPases (adenosine triphosphatases) located in the *trans*-Golgi network, namely ATP7A and ATP7B [18,29,30]. Subsequently, copper ions are transported into the lumen of the Golgi apparatus and loaded onto copper-dependent proteins and enzymes [30]. To identify copper-binding protein with potential relevance to traumatic brain injury, we used previously label-free liquid chromatography–mass spectrometry (LC–MS) proteomic analysis and identified copper-binding proteins showing differential expression through comparison with sham-treated brain tissues. Our analysis shows that, regarding Atox1, it shows a downward trend after traumatic brain injury. Given its crucial role in copper ion uptake, transportation and delivery, this may further impact the mitochondrial antioxidant capacity and cellular oxidative stress status. Additionally, recent researches have demonstrated the crucial role of Atox1 in the nervous system, specifically in regulating copper ion metabolism within neurons [31,32]. This function holds significant implications for both neuroprotection and neurodevelopment. Furthermore, multiple studies suggest that Atox1 may also play a role in neuronal apoptosis and various neurodegenerative diseases [33]. It should be noted that current researches on the correlation between Atox1 and mitochondria is still in its preliminary stages, leaving many questions unanswered. Further investigation is necessary to elucidate the intricate mechanisms underlying the role of Atox1 in regulating mitochondrial function, neurological disorders, and oxidative stress response.

DJ-1, also known as PARK7, is a 19.9 kDa protein that plays a crucial role in various neurological diseases, particularly its association with Parkinson's disease [34,35]. DJ-1 is implicated in several cellular processes, including the regulation of cellular oxidative stress [36], mitophagy [37], cell death [38] and protein repair [39], and may potentially exert a neuroprotective role through these mechanisms. In addition, researches have substantiated the importance of the interaction between DJ-1 and copper ions in regulating intracellular copper ion homeostasis and maintaining cellular function [40,41].

In this experiment, we systematically characterized the neuroprotective effect of Atox1 following craniocerebral trauma. Our findings demonstrated that Atox1 mitigates neuronal apoptosis in the hippocampal region by attenuating oxidative stress levels and facilitates recovery of neural functions such as memory and cognition. We have developed a co-immunoprecipitation protocol to identify Atox1 interaction partners following nerve injury, and our findings reveal a previously unrecognized interaction between Atox1 and DJ-1. Finally, we demonstrated that only Atox1 with copper-binding capacity interacts with DJ-1 as a means of reducing cellular oxidative stress levels.

2. Materials and methods

2.1. Reagents

Annexin V-FITC Apoptosis Detection Kit (Invitrogen, China), Ammonium tetrathiomolybdate (TTM) (Sigma-Aldrich, USA), TUNEL assay (Beyotime, China), ROS Assay kit (Beyotime, China), ROS Fluorescent Probe Kit (KeyGEN, China), MDA Assay Kit (Beyotime, China), GSH and GSSG Assay Kit (Beyotime, China), Tempol (Sigma-Aldrich, USA), Cell Counting Kit-8 (Dojindo, Japan), DCFH-DA (Beyotime, China), MitoSOX Red (Invitrogen, China), JC-1 (Invitrogen, China), Mito-Tracker Red, Mito-Tracker Green and Lysosome-Tracker Red (Invitrogen, China), Cell mitochondria isolation kit (Beyotime, China), Superoxide Dismutase Activity Assay kit (ab65354; Abcam).

Antibodies were from various sources, including GAPDH (5174; Cell Signaling Technology), Atox1 (22641-1-AP; Proteintech), Atox1 (ab154179; Abcam), NeuN (ab177487; Abcam), Cleaved Caspase-3 (9661; Cell Signaling Technology), Bax (ab32503; Abcam), Bcl-2 (ab182858; Abcam), DJ-1 (ab76008; Abcam), TOMM20 (ab283317, Abcam), TOMM20 (ab186735, Abcam), LC3-II (ab192890, Abcam), SQSTM1/p62 (ab109012, Abcam), PINK1 (23274-1-AP, Proteintech), PRKN (14060-1-AP, Proteintech), COX4 (11242-1-AP, Proteintech), FLAG (ab205606; Abcam).

2.2. Experimental animal

The Laboratory Animal Center of Nanjing Medical University provides adult male C57BL/6J mice weighing 25 ± 2 g. All animals were housed in a specific pathogen-free (SPF) environment with regulated temperature (22 ± 2 °C), a light-dark cycle of 12:12 h, and had ad libitum access to standard laboratory animal feed and water. The research protocols and animal experiments conducted in this study were approved by the Institutional Animal Care and Use Committee of Nanjing Medical University, following the guidelines set forth by the Animal Care and Use Committee (National Institutes of Health Publication No. 85–23, revised 1996).

2.3. Controlled cortical impact (CCI) model

As previously described [42], 8-week-old mice underwent surgery to establish a CCI model. The mice were anesthetized with 4 % isoflurane in a mixture of 70 % nitrous oxide and 30 % oxygen, and maintained under anesthesia with 1.5 % isoflurane. Body temperature was carefully maintained at 37 ± 0.5 °C using a heating blanket. Subsequently, a craniotomy with a diameter of 4 mm was performed on the left parietal bone (relative coordinates center of craniotomy to bregma: posteriorly by 1.5 mm and laterally by 2.5 mm). For the sham groups, only the dura mater was exposed without any further intervention. In the CCI groups, the exposed dura mater was impacted by an impactor at a velocity of approximately 6.0 ± 0.2 m/s, reaching a depth of approximately 1.4 mm for a dwell time of approximately 50-ms duration. After completing the injury procedure, the skin incision was closed, and then mice were placed back into their cages.

2.4. Virus and hippocampal injection

Hippocampal injection was performed as described previously [43]. Mice were transfected with a vector (AAV2-hSyn-cre-EGFP, GeneChem, China) containing either the mouse Atox1 gene or a construct harboring $Atox1^{12S15S}$ at the following coordinates: bromega 2.3 mm, L 1.8 mm, V 2.0 mm. The titer of the virus was 1×10^{13}, 2 μl was injected at a flow

rate of 0.5 μl/min (infusion time 4 min). The needle was left in place for at least 1 min after injection to allow virus distribution before removal. In that study, 14 days post-viral injection, mice underwent CCI, and 21 days post-viral injection, mice were utilized for subsequent experiments including immunofluorescence analysis, Western blotting, and behavioral assessments.

2.5. Brain tissue preparation

To prepare brain tissue, mice from each group were randomly selected following experimental TBI. The mice were anesthetized with 10 % chloral hydrate (0.4 mL/100 g) administered intraperitoneally. After successful anesthesia induction, the mice were positioned supine on a wooden board. A midline incision was made in the sternum to expose the chest cavity, and subsequently, the xiphoid process was elevated. Next, the right atrial appendage was severed and a perfusion needle was inserted through the apex of the left ventricle. Pre-cooled phosphate-buffered saline (PBS) solution was then gently perfused into both lungs and liver until their color turned grayish-white. Some animals were re-infused with 4 % paraformaldehyde depending on the type of experiment. Finally, the mouse was decapitated to expose and separate the skulls, and the brains were gently removed. Cerebral cortical tissues surrounding the lesions were collected, quickly frozen on dry ice, and then stored at - 80 °C for liquid chromatography-mass spectrometry (LC-MS) analysis and Western blot analysis. For immunostaining, brain tissues were fixed in neutral formalin solution for 24 h, then dehydrated with an alcohol gradient, and finally embedded in paraffin.

2.6. Y-maze test

The Y-maze apparatus was composed of three identical arms made of blue plastic, each measuring 44 cm in length and 15 cm in width, with walls standing at a height of 10 cm. This design allowed the mice to observe distal spatial landmarks. The test capitalizes on the innate inclination of mice to explore unfamiliar environments. Three arms were randomly assigned as the starting arm, novel arm, and other arm. In the training trial, the novel arm was physically obstructed. The mice were positioned in the start arm with their heads oriented away from the central area of the maze and given a 10-min opportunity to explore the alternate arm. Following a 1-h interval, the mice were reintroduced to freely navigate through all three arms of the maze for 5 min (test trial). All trials were meticulously captured by means of video recording. The number of entries into each arm, as well as the time spent and distance traveled within each arm, were precisely determined based on analysis of these recorded videos. Subsequently, percentages representing these three parameters relative to their respective totals were calculated. Additionally, comprehensive records encompassing total traveling distance and average speed were maintained.

2.7. Morris water maze (MWM) test

The experiments were conducted in a white circular pool with a diameter of 2.0 m, and the light intensity above the center of the pool was approximately 2.0 m. The pool was divided into four quadrants, and the average data from these quadrants represented the sample data. The water temperature was maintained at 22 ± 1 °C, and during hidden training sessions, its color was made opaque using non-toxic white paint. After a one-day period of individual handling to acclimate them to the introduction and removal from the pool, mice (n = 8–10/group) underwent a 5-day hidden training session consisting of four trials per day. During these sessions, the platform was positioned at a depth of 0.5–1.0 cm below the water surface. Time MWM software (TOPSCAN G3; ANY-MAZE 6.0.) was utilized to measure latency to reach the platform (s), swimming distance (cm), and swimming speed (cm/s) for each trial. The pool was surrounded by four distinct objects of different geometries, which served as spatial cues. Data were recorded when the mouse successfully located the platform. In cases where mice failed to find the platform within 60 s, they were guided towards it and required to stay on platform for 10 s, with a recorded latency of 60 s. Subsequently, the mice were placed in a heated cage equipped with a heating pad for drying before being returned to their home cage. The starting position was randomly changed to prevent track memorization, while the location of the platform remained constant throughout the experiment. A probe trial was conducted six days after the final spatial acquisition session to assess long-term memory following the treatments. The platform was removed from the target quadrant, and the mouse was placed in the starting position opposite to the original platform position, and allowed to swim for 60 s. Subsequent data, including escape latency during spatial acquisition sessions, latency to first crossover at the target site (probe time), number of crossovers at the platform site during the probe trial, percentage of time spent in the target quadrant during the probe trial, and percentage of distance traveled in the target quadrant during the probe trial were analyzed using Time MWM software.

2.8. Inhibitory avoidance test

The experimental procedure was conducted in accordance with previous descriptions [44]. Individual mice were placed in the brightly lit chamber, with an open-door hole connecting to the dark chamber, and allowed to freely explore both chambers for a duration of 5 min before being removed and returned to their rearing cage. Subsequently, the dark chamber was activated, and the time taken for mice to reach the middle of this chamber (training latency) was automatically measured using an infrared detection system. Following a 3-s delay, mice received a mild foot shock (125 V, 2 SEC, 0.2–0.4 mA). Ten seconds after receiving the shock, they were removed from the apparatus and returned to their rearing cage. Twenty-four hours post-training session, mice were once again placed in the bright chamber and scored based on their latency to enter into the dark compartment (maximum score: 300 s; test latency).

2.9. Cell culture and in vitro TBI model

HT22 cells (Shanghai Institute of Cell Biology, China) were cultured in Dulbecco's modified Eagle's medium (DMEM) (Gibco, USA), supplemented with 10 % fetal bovine serum (FBS) and 1 % penicillin-streptomycin antibiotics (Gibco, USA), under a controlled environment of 5 % CO_2 at 37 °C.

The in vitro TBI was conducted using a well-established mechanical stretch injury model, which employs a controlled pulse of compressed nitrogen gas to transiently deform the silastic membrane and achieve a predetermined level of stretching. The parameters for inducing moderate stretch injury were set at 28 psi with a duration of 50-ms, resulting in a peak pressure of 10.2 psi at the well site. Uninjured cells were utilized as control samples.

2.10. Lentiviral transfection

Atox1 mRNA sequence was obtained from NCBI: ATGCCGAAGCACGAGTTCTCCGTGGACAT GACCTGTGAGGGCTGTGCTGAAGCCGTCTCCAGAGTCCTCAACAAGCTGGGAGGAGTGGAGTTCAACATTGACCTGCC CAACAAGAAGGTCTGCATCGACTCTGAGCACAGCTCAGACACCCTGCTG GCAACCCTCAACAAAACAGGAAAGGCTGTTTCCTACCTTGGCCCCAAGT AG. Lentiviruses carrying Atox1 (pLV-Ef1a-Puro), Atox1 (pLV-Ef1a-3FLAG-Puro) or Atox112S15S (pLV-Ef1a-3FLAG-Puro) were obtained commercially from Genepharma (Shanghai, China).

For stable lentivirus transfection in primary neurons, cells were cultured in six-well plates using neural basal medium. Lentivirus was then introduced to the medium at a multiplicity of infection (MOI) of 100. Following a 72-h incubation period, fresh medium supplemented with puromycin (50 μg/mL) was added to facilitate stable cell selection.

The effects of gene overexpression or interference were subsequently validated through qRT-PCR and Western blot assays.

2.11. Small interfering RNA (siRNA) transfection

The Park7 siRNA was procured from Genepharma (Shanghai, China) and transfected following the manufacturer's instructions. Briefly, cells were seeded in 6-well plates using antibiotic-free growth medium one day prior to transfection. The Park7 siRNA was pre-complexed with Lipofectamine RNAiMAX (Invitrogen) and then added to the cell culture medium at a final concentration of 100 nM. After 48 h of incubation, the transfection medium was replaced with fresh medium. qRT-PCR and Western blot analyses were employed to assess the expression of Park7 protein in the siRNA-transfected cells.

2.12. Relative quantitative RT-PCR

The relative quantitative RT-PCR was conducted in accordance with our previous investigations [42]. The primers were listed as follow:

Atox1, Forward primer (5 → 3) AAGCTGGGAGGAGTGGAGTT.
Reverse primer (3 → 5) CCTGTTTTGTTGAGGGTTGC;
Park7, Forward primer (5 → 3) CCAAAGGAGCAGAGGAGATG.
Reverse primer (3 → 5) CCTTAGCCAGTGGGTGTGTT.
SOD1, Forward primer (5 → 3) AGCGGTGTGCGTGCTGAAG.
Reverse primer (3 → 5) GTCCTGACAACACAACTGGTTCAC.
SOD3, Forward primer (5 → 3) TGGTTGAGAAGATAGGCGACACG.
Reverse primer (3 → 5) CATCTCGGCAGCATCCACCTC.
Gapdh, Forward primer (5 → 3) AGAAGGTGGTGAAGCAGGCATC.
Reverse primer (3 → 5) CGAAGGTGGAAGAGTGGGAGTTG.

2.13. Terminal deoxynucleotidyl transferase mediated dUTP nick end labeling (TUNEL) assay

TUNEL assay were performed as described previously [45].

2.14. Brain tissue reactive oxygen species detection

We employed the ROS Assay kit (Beyotime, CN), comprising primarily of the fluorescent probe DHE (dihydroethidium), to assess levels of O_2^-, which is a reactive oxygen species (ROS) with strong oxidation, in cryosections of the hippocampal region. Upon exposure to O_2^-, the DHE probe undergoes oxidation, resulting in the generation of a red fluorescent compound whose intensity is directly proportional to O_2^- concentration. The experimental protocol involved utilization of a 2 μM working solution of DHE. Fluorescence imaging was performed using a Carl Zeiss Microscopy fluorescence microscope (Germany) with excitation at 535 nm and emission at 610 nm wavelengths. Mean fluorescence intensity (MFI) measurements for DHE were quantified using Image J software.

2.15. Tempol preparation and dosing

Tempol (Sigma-Aldrich, USA) was used to test whether DHE signals in brain tissue could be specifically eliminated. The CCI-treated mice were treated with Tempol (intraperitoneal injection, 300 mg/kg) as described previously [46]. Saline was also used as a control for the Tempol-treated group.

2.16. Cell viability

Viability of cells was determined using the Cell Counting Kit-8 (CCK-8, CK04, Dojindo, Tokyo, Japan) assay. Briefly, cells were cultured in a 96-well plate and incubated with the reagent at 37 °C for 2 h. Subsequently, optical density (OD) values were measured at 450 nm using a Thermo Multiskan FC microplate photometer.

2.17. Reactive oxygen species determination

DCFH-DA staining method (Beyotime, China) was employed to assess the levels of ROS. In brief, the collected cells were stained with 2.5 μM DCFH-DA for a duration of 30 min and subsequently washed twice with PBS. Following the washing steps, a cell count of 1×10^5 cells per sample was determined, and the ROS levels were measured using either confocal microscopy (Stellaris STED, Germany) or flow cytometry (GALLIOS, USA), as per the manufacturer's instructions.

2.18. Mitochondrial superoxide quantification

Cells were incubated with 5 μM MitoSOX Red (M36005, Invitrogen) for a duration of 10 min, followed by washing with warm PBS to eliminate any excess dye. To visualize the stained cells, random fields in each group were captured using confocal microscopy (Stellaris STED, Germany). The acquired data was subsequently analyzed utilizing ImageJ software.

2.19. TMRM assay

Mitochondrial membrane potential was assessed by fluorescence mitochondrial imaging using TMRM (I34361, Invitrogen, China). HT-22 cells were incubated with TMRM solution at 37 °C for 30 min. Subsequently, the cells were washed twice with PBS. Confocal microscopy (Stellaris STED, Germany) was employed to capture images. The intensity of fluorescence indicates the level of mitochondrial membrane potential.

2.20. Transmission electron microscopy (TEM)

Brain tissues or HT-22 cells were fixed in PBS (pH 7.4) containing 2.5 % glutaraldehyde for at least 1 h at room temperature. Following this step, the brain tissues or HT-22 cells were post-fixed with 1.5 % osmium tetroxide for 2 h at a temperature of 4 °C and subsequently dehydrated using ethanol before being embedded in epoxy resin. The ultrastructure was observed by transmission electron microscopy (Quanta 10, FEI Co.) on ultrathin sections measuring approximately 70 nm.

2.21. Mitochondrial fluorescent staining

Mitochondria in HT-22 cells were simultaneously labeled using Mito-Tracker Red. The mean fluorescence intensity (MFI) and the mean grey values (MGV) were analyzed using Image J software.

2.22. Determination of malondialdehyde (MDA), GSH and GSSG levels

The levels of MDA, GSH, and GSSG were quantified following the previously described methodology [45].

2.23. Mitochondria isolation

After different treatments, HT-22 cells were harvested and then isolated according to the manufacturer's protocol for the cell mitochondria isolation kit (Beyotime, C3601). Briefly, cells were resuspended in a mitochondria extraction reagent and homogenized using a microhomogenizer. Subsequently, they were incubated on ice for 15 min. The resulting homogenates were centrifuged at 600 g for 10 min at 4 °C, followed by collection of the supernatants which underwent further centrifugation at 11,000 g for 10 min at 4 °C. The mitochondrial fraction was isolated from the sediment and subsequently subjected to co-immunoprecipitation assay after mitochondrial lysis to quantify the binding of Atox1 and DJ-1.

2.24. Co-immunoprecipitation (Co-IP) assay

Co-IP experiment was conducted according to the previously described protocol [47]. Briefly, HT-22 cells were lysed and total lysates were collected using a weak RIPA lysis buffer (Cell Signaling Technology, Danvers, MA, USA). After incubation with primary antibodies overnight at 4 °C at the appropriate dilution, the immune complexes were pulled down using protein A/G agarose on a shaker for 4 h at 4 °C. The microbeads were then collected, washed, and the proteins were eluted by boiling in 1 × loading buffer for subsequent immunoblotting analysis.

2.25. Superoxide dismutase activity assay

The superoxide dismutase (SOD) activity was assayed utilizing the Superoxide Dismutase Activity Assay Kit (ab65354, Abcam), strictly adhering to the manufacturer's protocol. Specifically, SOD1 in cytoplasm lysates and SOD3 secreted into the culture medium were collected after stretch treatment. To procure cytoplasmic proteins with mitochondrial exclusion from HT-22 cells, the cell mitochondria isolation kit (Beyotime, C3601) was employed.

2.26. Statistical analysis

All data were analyzed using GraphPad 8.0 software and presented as the mean ± standard deviation (SD) of at least three independent

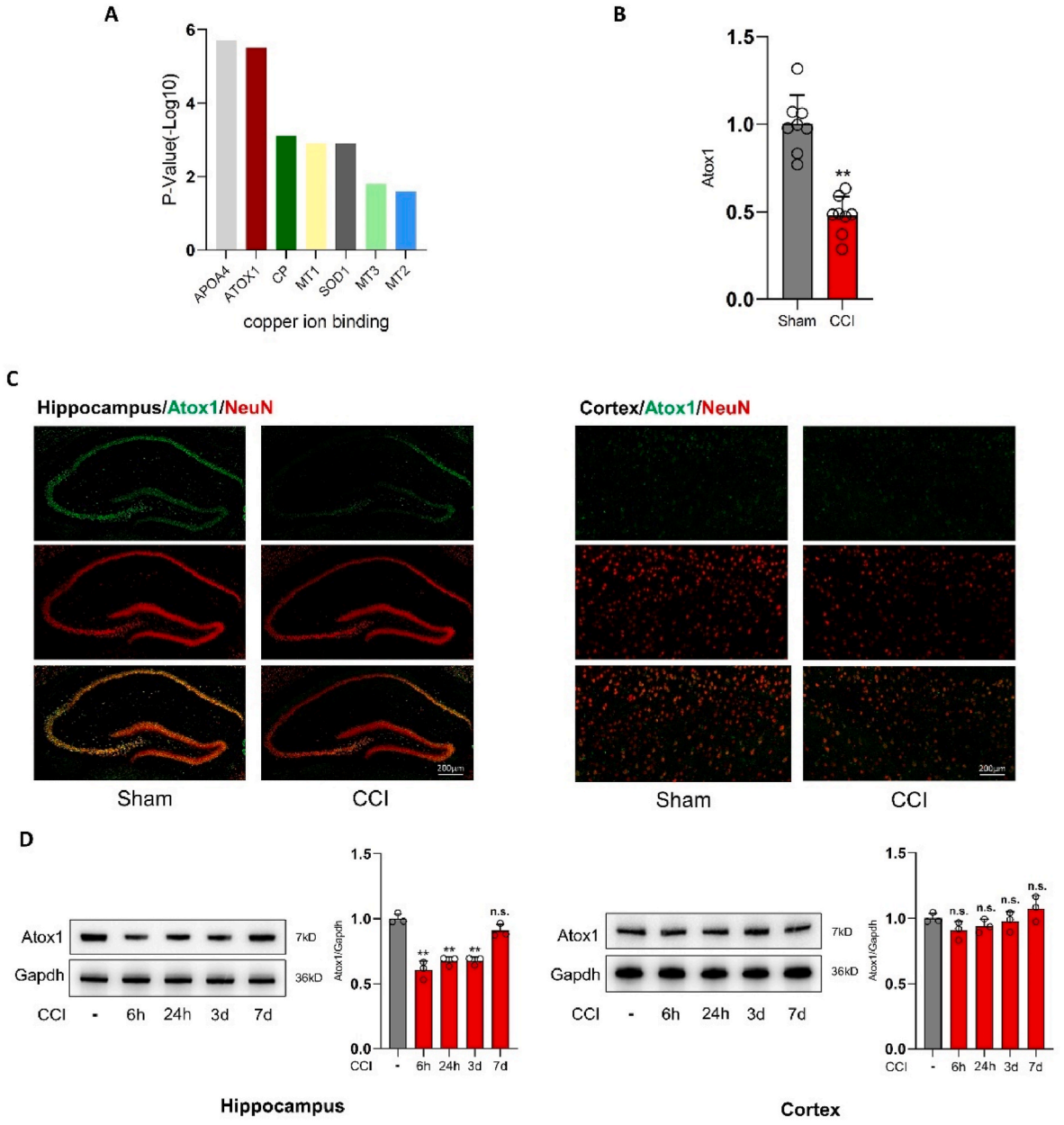

Fig. 1. Atox1 expression was down-regulated in the hippocampus, but not in the cortex, following TBI. (A) The rank plot of seven most valuable copper binding proteins, according to the *P*-value. (B) The relative protein level of Atox1 in CCI (n = 8) vs. sham according to LC–MS proteomic analysis (n = 8). (C) Representative images of immunofluorescence staining of Atox1 (Green) and NeuN (Red) in hippocampal or cortical region (Scale bar is 200 μm, n = 3). (D) Western blot images of Atox1 protein in hippocampal or cortical region, and the statistical results (n = 3). Values represent the mean ± standard deviation (SD). *P < 0.05 vs. sham group, **P < 0.01 vs. sham group, and n.s.: no significant difference.

experiments. Grey levels and fluorescence intensities were measured using ImageJ software. Statistical analysis was performed using an unpaired Student's t-test or one-way analysis of variance (ANOVA) followed by Tukey's post hoc test to compare differences between two groups. For comparisons among multiple groups at the same time point, a one-way ANOVA followed by Tukey's post hoc test was used. Two-way ANOVA was employed to compare data across all groups. A significance level of $P < 0.05$ was considered statistically significant.

3. Results

3.1. Atox1 expression was down-regulated in the hippocampus, but not in the cortex, following CCI

Previous studies have reported that copper binding proteins and copper ion delivery have an important role after TBI [48]. In our previous study, we qualitatively and quantitatively analyzed the changes in the content of all 2499 proteins in mice after CCI, and we found statistically significant changes in the levels of 7 copper-binding proteins after CCI, including SOD1, an antioxidant protein that has been studied extensively (Fig. 1A and B, Suppl. Fig. 1A). Moreover, among these copper ion-binding proteins, Apoa4 and Atox1 showed the most statistically significant changes in protein levels (Fig. 1A). By reviewing the Brain-seq database, we found that Apoa4, although partially mentioned in studies of the central nervous system (CNS), was not transcribed in the main cells of the central nervous system, such as neurons and glial cells, in either humans or mice; in contrast, Atox1 was at high transcriptional levels in various cells of the human central nervous system, with the highest transcriptional levels in neurons, and in the mouse central nervous system, the highest transcriptional levels in endothelial cells (Suppl. Fig. 1B). Moreover, we examined several crucial Cu transport and chaperone proteins in our LC–MS proteomic analysis, such as Ctr1, ATP7A, and CCS. Our findings revealed a non-significant decrease in Ctr1 and CCS levels following CCI, while ATP7A was not detected due to its low abundance in CNS (Suppl. Figs. 1C and D). Given our attempt to investigate the mechanisms of CNS protection and neural repair after TBI, Atox1 is more in line with our research direction.

Based on our LC–MS proteomic analysis, it was demonstrated that there was a significant decrease in the level of Atox1 after CCI compared to the sham-operated group (Fig. 1B). In addition, we performed immunofluorescence double-label staining on brain tissue sections. We found that in hippocampal neurons, the fluorescence intensity of Atox1 after CCI was significantly reduced compared to the sham-operated group. Conversely, there was no significant change in the fluorescence intensity of Atox1 in cortical neurons after CCI (Fig. 1C). This led us to continue to explore whether the temporal dynamics of Atox1 protein expression after CCI were statistically different in cortical and hippocampal regions. The results of Western blot analysis demonstrated that the levels of Atox1 protein in the hippocampal region exhibited a significant decrease at 6 h, 24 h, and 3 days after CCI, gradually approaching pre-CCI levels by day 7. Conversely, no significant changes were observed in Atox1 protein levels within the cortex during the entire 7-day period following CCI. (Fig. 1D). The reason that downregulation of Atox1 by CCI treatment was not observed in the cerebral cortex may be due to the higher content of endothelial and glial cells in the cerebral cortex; according to Suppl. Fig. 1B, Atox1 content was higher in endothelial and glial cells than in neuronal cells in mice, and the alteration in Atox1 content in endothelial and glial cells may not significant following CCI. Given the presence of a large number of neuronal cells in the hippocampal region and this region involved in various sensory, and cognitive function [49], we focused on the role of Atox1 in hippocampal neurons in the remainder experiments.

3.2. Atox1 overexpression ameliorates hippocampal neuron apoptosis and oxidative stress in CCI-treated mice

To determine the role of Atox1 in the CCI model, we first performed AAV-Atox1 transfection of the hippocampal region and examined Atox1 transfection 14 days later (Suppl. Figs. 2A and B), followed by CCI.

Considering the contribution of apoptosis in the pathogenesis of craniocerebral injury, evidences demonstrated that severe craniocerebral injury causes massive neuronal apoptosis. Therefore, we first analyzed whether overexpression of Atox1 has an effect on neuronal apoptosis. Compared with the sham-operated mice, CCI-treated mice exhibited a higher number of TUNEL-positive neuronal cells, while overexpression of Atox1 decreased the apoptotic rate significantly (Fig. 2A). The CCI treatment resulted in an upregulation of cleaved caspase-3 and Bax protein expressions, while downregulating the expression of Bcl-2 protein. Conversely, Atox1 overexpression led to a decrease in apoptosis-related proteins and an increase in anti-apoptotic protein expression compared to the CCI group (Fig. 2B). In addition, the thickness of the cell layer in the hippocampal region, as assessed by NeuN staining, was significantly decreased in the mice 3 months after CCI, and this thickness was highly correlated with hippocampal volume. However, the CCI + Atox1 group showed more neuronal staining as well as the thickness compared with the CCI group (Fig. 2C).

Evidences demonstrated that Atox1 plays an important role in antioxidant responses [31], we detected the levels of oxidative stress in the hippocampal region to further explore the anti-oxidative effects of Atox1. The results demonstrated a significant increase in the levels of MDA and GSSG in the hippocampus of the CCI-operated mice, whereas overexpression of Atox1 led to a reduction in MDA and GSSG levels. Conversely, it resulted in an elevation of GSH level (Fig. 2D). In addition, ROS staining revealed an increase in hippocampal ROS production in CCI-operated mice. However, the overexpression of Atox1 significantly alleviated ROS production (Fig. 2E). Simultaneously, because the DHE fluorescence signal is specific for superoxide anion, we administered Tempol, a superoxide dismutase (SOD) mimic known for its efficient scavenging ability against superoxide anion, via intraperitoneal injection (300 mg/kg) in CCI -treated mice. We found that the DHE fluorescence signal in brain tissue was specifically eliminated by Tempol, which confirmed that Tempol reversed O2- production following CCI (Suppl. Figs. 2C and D).

3.3. Increased level of Atox1 improves learning and memory performance after CCI

Since Atox1 reversed the neuronal apoptosis and inhibits oxidative stress, we further assessed in vivo effect of Atox1 on CCI-induced phenotype development. We initially examined the disparities in survival rates between the groups. Our findings revealed that, in comparison to the sham group, the CCI group exhibited a significantly diminished survival rate. Although lacking statistical significance, Atox1 overexpression subsequent to CCI demonstrated an enhanced survival rate when compared to mice subjected to CCI (Fig. 3A).

We subsequently conducted a series of behavioral experiments to assess the impact of Atox1 on the neurocognitive capacity of mice following CCI. Initially, we conducted the Y-maze test to evaluate short-term working memory in each group of mice [50]. Notably, during the trial phase, mice in the CCI group exhibited a significantly lower frequency of entering the novel arm compared to those in the sham-operated group. However, overexpression of Atox1 resulted in an increased frequency of mice entering the novel arm (Fig. 3B). Consistently, the latency time and distance of CCI + Atox1 mice in the novel arm were also significantly longer than those in the CCI group (Fig. 3C and D). The heatmaps depicting the trajectories of each group during the trial phase are shown in Fig. 3E. In addition, the statistical analysis revealed no significant disparity in total distance and average speed among the groups, indicating that there was no dyskinesia across all

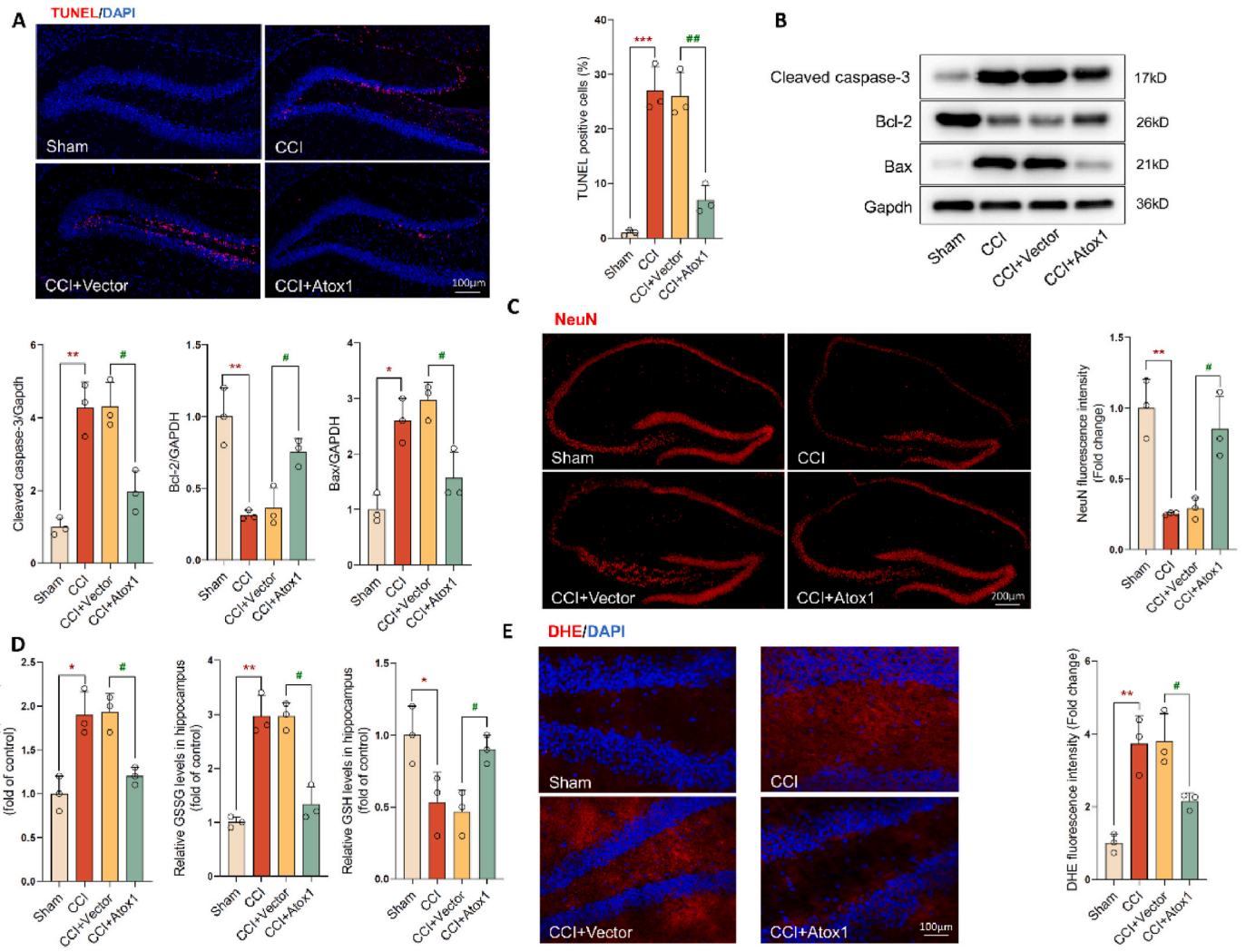

Fig. 2. Atox1 overexpression ameliorates hippocampal neuron apoptosis and oxidative stress in CCI-treated mice. (A) Representative images of TUNEL staining in hippocampal region and relative quanti-fication (Scale bar is 100 μm, n = 3). (B) Western blot images of Cleaved caspase-3, Bcl-2 and Bax in hippocampus region, and the statistical results (n = 3). (C) Representative images of immunofluorescence staining of NeuN (red) in hippocampal region and relative quantification. (Scale bar is 200 μm, n = 3). (D) The levels of MDA, GSSG, and GSH (n = 3). (E) Representative images of DHE fluorescence staining in hippocampal region and relative quantification (Scale bar is 100 μm, n = 3). Values represent the mean ± standard deviation (SD). *P < 0.05 vs. sham group, **P < 0.01 vs. sham group, ***P < 0.001 vs. sham group, #P < 0.05 vs. CCI + Vector group, ##P < 0.01 vs. CCI + Vector group.

mouse cohorts (Fig. 3F and G). Subsequently, the Morris water maze test was employed to evaluate the spatial learning aptitude and long-term working memory capacity of mice post CCI [50]. During 5-day of spatial acquisition period, we assessed escape latency, which is defined as the time taken by mice to locate a hidden platform. While the sham-operated mice exhibited a decrease in escape latency over five consecutive training days, with significant reduction value on day 5 compared to initial value, whereas the CCI-operated mice continued to exhibit prolonged escape latencies even on day 5. Specifically, their escape latency was 2.2 times longer than that of the sham-operated group, indicating impaired learning in these mice. However, the situation was improved and the escape latency was significantly reduced with subsequent Atox1 overexpression following CCI (Fig. 3H). In addition, the statistical analysis revealed no significant disparity in average speed among the groups, indicating that there was no dyskinesia across all groups of mice (Fig. 3I). Fig. 3J displays the motion curves observed on the 5th day of hidden training session. After the completion of the spatial acquisition period, the mice underwent memory testing. The hidden platform was removed and the mice were observed to explore both the duration and trajectory within the pool. The results indicated that mice subjected to CCI exhibited reduced time spent in the target quadrant and fewer crossings of the platform compared to sham-operated mice, while overexpression of Atox1 partially restored these conditions (Fig. 3K and L). The heatmaps depicting the trajectories of each group during the probe trial phase are shown in Fig. 3M. Finally, we conducted the step-through passive avoidance test to assess the memory retention ability of mice following CCI [44]. There was no significant difference in latency observed between the groups during the training phase (1st trial). However, during the testing phase (2nd trial), a trend of improvement in latency was noted in the sham group, which was significantly lower when compared to the CCI group (Fig. 3N). The motion curves on the 1st trial and the 2nd trial are shown in Fig. 3O.

Together, the findings of the memory-related behavioral tests indicated that overexpression of Atox1 exhibits efficacy in ameliorating both short- and long-term memory impairments in mice subjected to CCI.

3.4. *Atox1 overexpression reduces the apoptosis and oxidative stress level in stretch-treated HT-22 cells*

To further validate the role of Atox1 in neuroprotection, we initially investigated the temporal dynamics of Atox1 protein expression and its subcellular localization in HT22 cells following stretch injury model. As

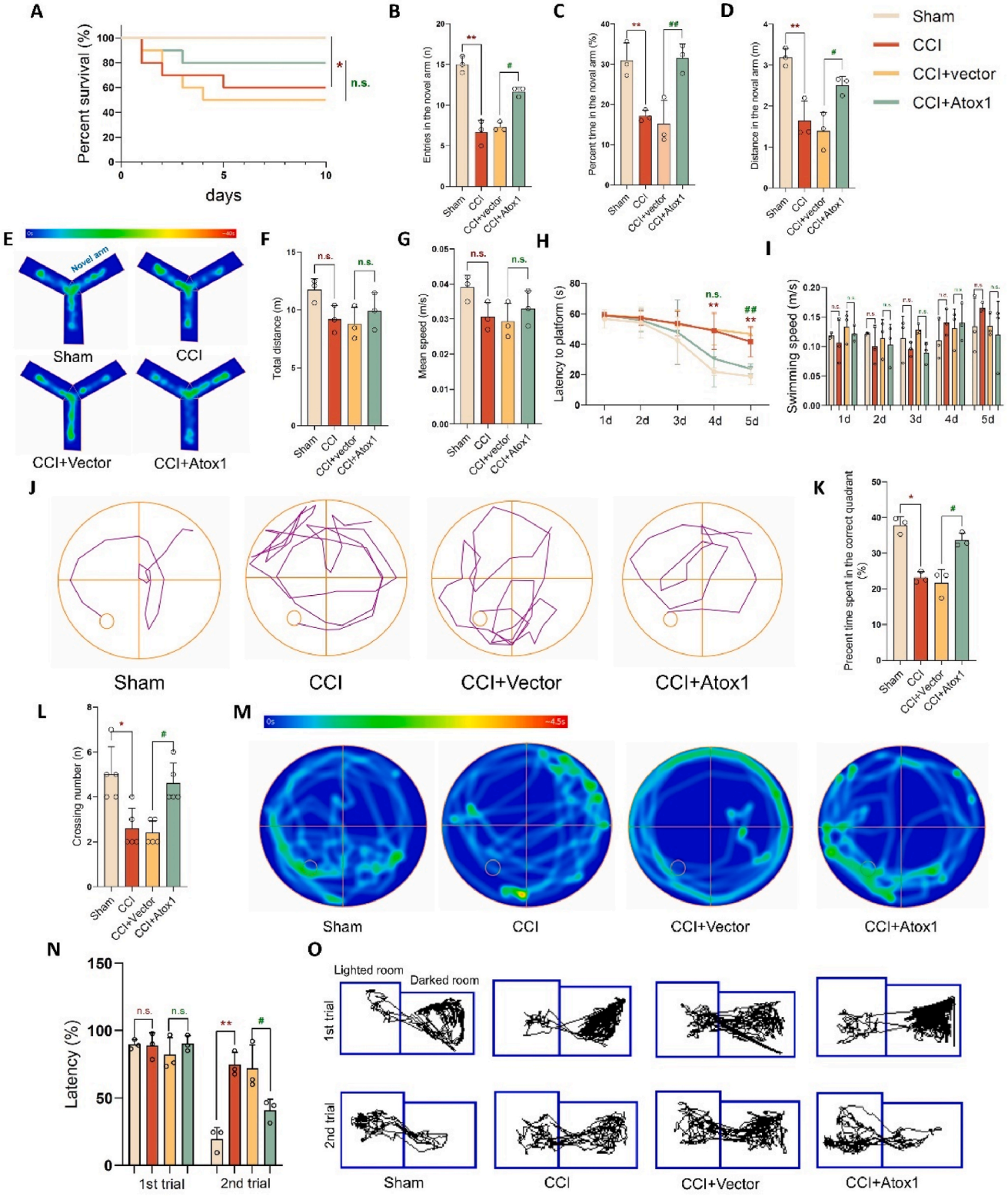

Fig. 3. Increased level of Atox1 improves learning and memory performance after CCI. (A) Kaplan-Meier curve of 10-day survival in mice (n = 10). (B–D) The percentage of entries, distance and time in the novel arm over all the arms during the test trial phase (n = 3). (E) Representative heatmap of tracks during the test trial phase. (F–G) Total distance and the average speed of the animals traveled in all the arms (n = 3). (H) The latencies to platform in the four groups over five consecutive training days (n = 3). (I) The swimming speed in the four groups over five consecutive training days (n = 3). (J) Representative swimming tracks of the mice in all four groups on the 5th day during the training days. (K) The percentage of time spent in the target quadrant during the probe trial (n = 3). (L) The average crossing number over the platform-site during the probe trial (n = 5). (M) Representative heatmap of tracks during the probe trial. (N) The percentage of time spent in a darked room during the training trial and test trial (n = 3). (O) Representative tracks of the mice in all four groups during the training trial and test trial. Values represent the mean ± standard deviation (SD). *P < 0.05 vs. sham group, **P < 0.01 vs. sham group, #P < 0.05 vs. CCI + Vector group, ##P < 0.01 vs. CCI + Vector group, and n.s.: no significant difference.

shown in Fig. 4A, the level of Atox1 in stretch-treated HT-22 cells exhibited a significant decrease at 6 h, which was sustained for at least 24 h and gradually restored to the baseline level after 3 days. Subsequently, immunofluorescence assay was employed to investigate the subcellular localization of Atox1 in wild-type and stretch-treated HT-22 cells. We observed that the fluorescence signal of Atox1 predominantly co-localized with the mitochondria marker TOMM20 and nuclear marker DAPI, while no significant co-localization was observed with Calnexin (an endoplasmic reticulum marker), RPS3 (a ribosome marker), or LAMP1 (a lysosome marker) in wild-type HT-22 cells. Following stretch injury, there was a substantial increase in the co-localization of Atox1 with mitochondria and maintained a consistently high percentage of colocalization for at least 3 days, whereas its co-localization with the nucleus remained unchanged and minimal association with other organelles was detected (Fig. 4B, Suppl. Fig. 3A). Then, HT-22 cells were transfected with lentivirus to upregulate Atox1 (Suppl. Figs. 3B and C), and subsequent cell viability experiments were conducted in both wild-type and Atox1-upregulated cells following stretch treatment. We observed a significant decrease in cell viability upon stretch injury, whereas Atox1 overexpression led to an improvement in cell viability in HT-22 cells treated with stretch (Fig. 4C). The overexpression of Atox1 impeded apoptosis in stretch-treated HT-22 cells (Fig. 4D). Simultaneously, we observed a significant increase in the expression of cleaved caspase-3 and Bax, as well as a decrease in the level of Bcl-2 in HT-22 cells following stretch injury, which were subsequently restored upon upregulation of Atox1 (Fig. 4E).

We also investigated whether infection with lentivirus overexpressing Atox1 could suppress the oxidative stress response. Compared to stretch-treated HT-22 cells, overexpression of Atox1 significantly diminished intracellular ROS levels in HT-22 cells (Fig. 4F). The flow cytometry analysis revealed a significant increase in the mean fluorescence intensity (MFI) of DCFH-DA in stretch-treated cells compared to control cells, while Atox1 overexpression effectively attenuated ROS levels in stretch-treated HT-22 cells (Fig. 4G). Consistently, the results obtained from MitoSOX Red staining demonstrated that Atox1 plays a crucial role in mitigating mitochondrial superoxide production (Fig. 4H). Furthermore, we assessed the mitochondrial membrane potential (MMP) using the TMRM assay. TMRM staining is employed for the monitoring of mitochondrial function. Upon accumulation within polarized mitochondria with a negative charge, TMRM exhibits an orange fluorescence. Conversely, in apoptotic or metabolically stressed cells where the mitochondrial membrane potential collapses, the TMRM reagent disperses throughout the cytosol of the cell and leads to a significant drop in fluorescence levels. As shown in Fig. 4I, stretch injury induced a reduction in MMP levels in HT-22 cells compared to the control group. However, the overexpression of Atox1 reversed this decline and restored mitochondrial membrane potential in stretch-treated HT-22 cells.

3.5. *Atox1 overexpression maintains mitochondrial structure and promotes mitophagy after stretch treatment*

The disruption of mitochondrial function and structure is a significant contributor to oxidative stress disorders, and we continue to explore the effects of Atox1 on mitochondrial function and structure. The expression of the mitochondrial proteins (TOM20 and TIM23) was significantly downregulated in the HT-22 cells treated with stretch compared to the control cells, whereas overexpression of Atox1 reversed the decrease in TOM20 and TIM23 contents in stretch-treated HT-22 cells (Fig. 5A). Furthermore, Atox1 effectively restored the ATP levels in HT-22 cells treated with stretch (Fig. 5B). To further investigate these changes, we utilized MitoTracker Red staining to examine mitochondrial structure in each group of HT-22 cells. As shown in Fig. 5C and D, stretch induced a shift in mitochondrial morphology from a filamentous network to a more punctate structure, accompanied by a reduction in total red fluorescence area indicative of mitochondrial contraction. However, Atox1 overexpression ameliorated the aberrant mitochondrial phenotype and increased fluorescence area. The morphological features of mitochondria were also quantitatively identified by ImageJ software and key aspects of mitochondrial morphology were captured [51]. Mitochondrial size was represented by mean area and mean perimeter, while mitochondrial shape was defined by form factor (FF) and aspect ratio (AR) for 2D analysis. Our findings suggested that stretch-treated cells exhibited poorer mitochondrial structure compared to the normal HT-22 cells, whereas Atox1 overexpression reversed the abnormal mitochondrial structure (Fig. 5E). Meanwhile, we assess the overall connectivity and morphological intricacy of the mitochondrial network based on the skeletonized network (Fig. 5F), quantifying these aspects through metrics such as branch count, branch junction count, and total (accumulated) branch length in the skeleton. As shown in Fig. 5G, compared to control HT-22 cells, HT-22 cells treated with stretch exhibited reduced branch length and fewer network connections in their mitochondria, which were restored to a normal structural network by the overexpression of Atox1.

We subsequently conducted transmission electron microscopy (TEM) to evaluate the impact of Atox1 on alterations in mitochondrial morphology. The mitochondria in the control group exhibited pristine conditions, characterized by intact structures and visible cristae (Fig. 6A, green arrowhead). Conversely, stretch-treated HT-22 cells displayed swollen mitochondria with aberrant morphology (Fig. 6A, red arrowhead), whereas overexpression of Atox1 tended to restore mitochondrial morphology to a more normal state in stretch-treated HT-22 cells (Fig. 6A, green arrowhead). Interestingly, isolated mitochondria in autophagosomes were observed in stretch-treated cells that overexpressed Atox1 (Fig. 6A, white arrowhead) , suggesting the presence of mitophagy. The immunolocalization of autophagosome marker LC3-II and mitochondria marker TOMM20 was conducted to further investigate the potential impact of Atox1 on mitophagy. It was observed that co-localization of LC3-II and TOMM20 fluorescence was evident in the Atox1+Stretch group, while minimal co-localization was observed in other groups, indicating a promotional role of Atox1 in mitophagy (Fig. 6B). Furthermore, the results of Western blot analysis showed that overexpression of Atox1 dramatically increased the LC3-II/I ratio, decreased the protein level of SQSTM1/p62, and enriched PINK1 and PRKN compared to stretch-treated cells (Fig. 6C).

Collectively, our findings demonstrate that Atox1 plays a crucial role in maintaining mitochondrial morphology and facilitating mitophagy for the elimination of damaged mitochondria.

3.6. *Atox1 may interact with another copper-binding protein after injury*

To investigate the potential mechanisms of Atox1 and evaluate its known and predicted protein interactions, we initially referred to the STRING database (String-db.org). By considering the lowest confidence score and all confidence hit rates, we observed a significant concentration of Atox1 interacting proteins in mitochondrial and antioxidant stress-related proteins (Fig. 7A). This observation further strengthens our conviction regarding the crucial role played by Atox1 in mitochondrial involvement during oxidative stress. Then, we performed co-immunoprecipitation (co-IP) followed by mass spectrometry (MS) analysis to obtain the set of proteins interacting with Atox1 in traumatized and non-traumatized brain tissue. And we applied GO enrichment analysis to assess the functions of these protein assemblies. We observed significant differences in both quantity and composition of anti-oxidative stress-related proteins between the two protein collections. In non-traumatic brain tissue, only two anti-oxidative stress-related proteins (Perm and S10a9) were found to interact with Atox1. However, in traumatic brain tissue, the number of anti-oxidative stress-related proteins binding to Atox1 increased to ten, including proteins Sod1, Park7, and Gpx4 (Fig. 7B).

Previous studies have demonstrated that the delivery of copper by Atox1 to downstream copper binding proteins plays a crucial role in

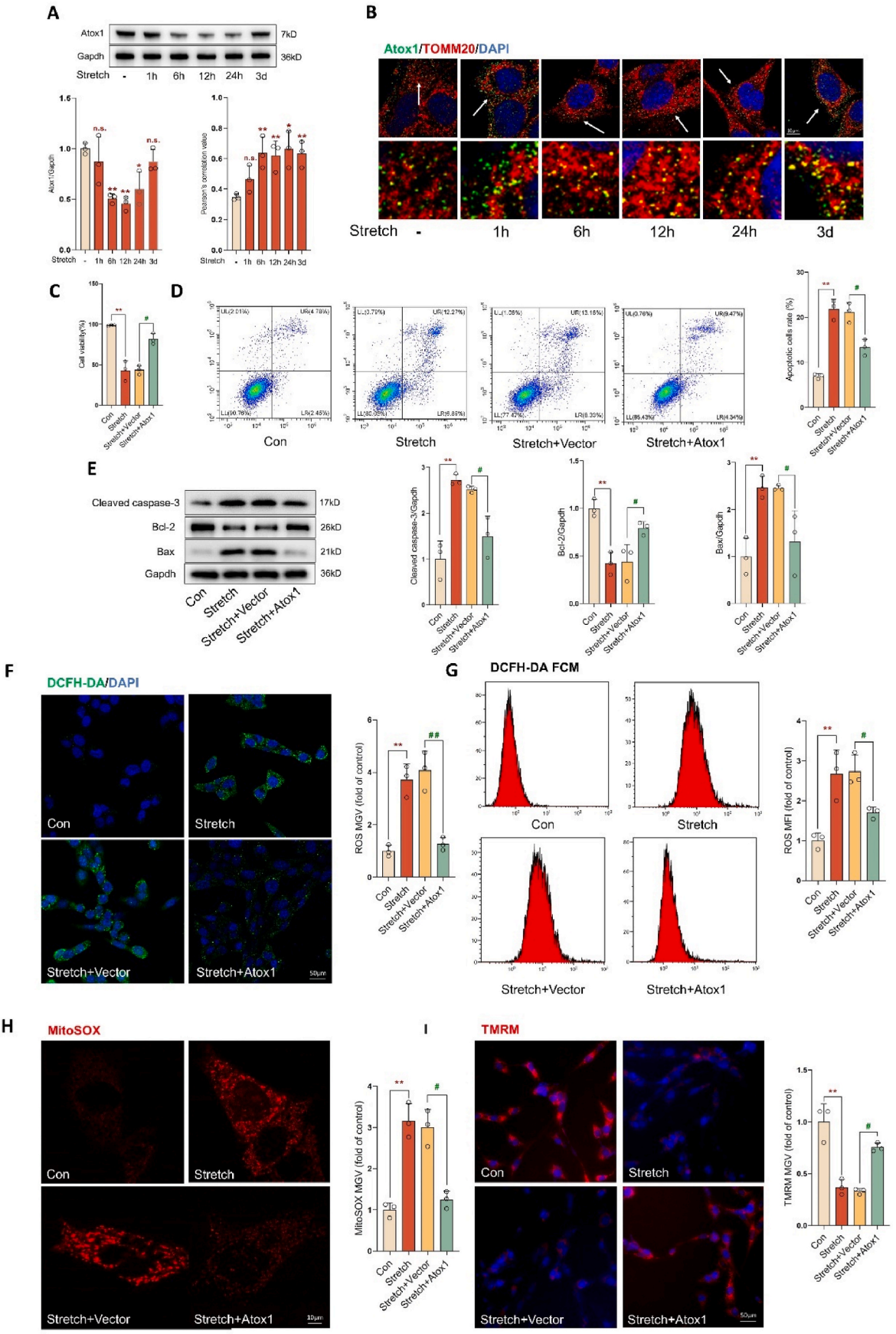

(caption on next page)

Fig. 4. Atox1 overexpression reduces the apoptosis and oxidative stress level in stretch-treated HT-22 cells. (A) Western blot images of Atox1 protein in wide-type and stretch-treated HT-22 cells, and the statistical results (n = 3). (B) Atox1 colocalizes with TOMM20 in wide-type and stretch-treated HT-22 cells. Statistical analysis involves calculating the Pearson's coefficient for colocalization of Atox1 and TOMM20 (white arrow represents the zoom area. Scale bar is 10 μm, n = 3). (C) Cell viability detected via CCK-8 assay kit (n = 3). (D) Cell apoptosis rate was determined using flow cytometry (n = 3). (E) Western blot images of Cleaved caspase-3, Bcl-2 and Bax in hippocampus region, and the statistical results (n = 3). (F, G) Representative images and flow cytometric analysis of ROS level, and relative quantification. (Scale bar is 50 μm, n = 3). (H) Representative images of MitoSOX staining, and relative quantification. (Scale bar is 10 μm, n = 3). (I) Representative images of TMRM staining, and relative quantification. (Scale bar is 50 μm, n = 3). Values represent the mean ± standard deviation (SD). **P < 0.01 vs. control group, #P < 0.05 vs. Stretch + Vector group, ##P < 0.01 vs. Stretch + Vector group.

cellular metabolism [52]. Recent reports have indicated that DJ-1 exhibits metal binding properties, such as copper and mercury, thereby implying a potential role of DJ-1 in cellular protection against metal-induced cytotoxicity [40,53]. Meanwhile, a comprehensive investigation into the copper binding kinetics of DJ-1 has been conducted, revealing specific amino acid residues (Cys106, Glu18, and Cys-53) as copper ligands. This finding unequivocally confirms DJ-1's role as a proficient copper chaperone capable of facilitating efficient copper delivery [41]. By referencing the microscopic structure of the DJ-1 protein in the Protein Data Bank (PDB DOI: https://doi.org/10.2210/pdb4mnt/pdb) and integrating it with relevant study [41], we have substantiated that copper ions play a crucial role in facilitating the biological functions of DJ-1. Furthermore, we have identified two cysteine residues (Cys-53) and two amino acid residues (Cys-106, Glu-18) as pivotal binding sites for copper ions within DJ-1. Our alignment of DJ-1 amino acid sequences in different species revealed that amino acid residues (cys-53, cys-106, glu-18) with copper binding ability are evolutionarily conserved, suggesting an important role in the regulation of DJ-1 function (Fig. 7D).

To sum up, we speculate that Atox1 and DJ-1 may have a synergistic effect in the same oxidative stress response pathway, which potentially based on a copper-mediated interaction between the two proteins.

3.7. Atox1 attenuates oxidative stress and promotes mitophagy via DJ-1

We initially investigated the expression of DJ-1 in HT22 cells following a stretch injury model. The results obtained from Western blot analysis demonstrated a consistently upregulation of DJ-1 expression in HT-22 cells subjected to stretch treatment (Suppl. Fig. 4A). Then, to confirm the interaction between Atox1 and DJ-1, we initially verified their co-localization in HT-22 cells through immunofluorescence staining. As shown in Fig. 8A, the proportion of Atox1 co-localized with DJ-1 was significantly higher in stretch-treated HT-22 cells than that in control HT-22 cells. Given the significantly increased colocalization of Atox1 with mitochondria in the stretch injury model compared to the wide-type groups (Fig. 4B), we further investigated the mitochondrial colocalization of Atox1 and DJ-1 following stretch treatment. As shown in Fig. 8B, our findings demonstrate that Atox1 exhibits colocalization with DJ-1 on mitochondria in stretch-treated HT-22 cells. Additionally, the mitochondrial proteins were individually isolated from control HT-22 cells and stretch-treated HT-22 cells. Co-immunoprecipitation assay was employed to analyze the binding of Atox1 to DJ-1, and the results shown that the interaction between Atox1 and DJ-1 in mitochondria is enhanced upon stretch treatment (Fig. 8C). Furthermore, we conducted an investigation into the interaction between Atox1 and DJ-1 in vivo CCI model, as well as the expression of DJ-1 protein. Consistent with our in vitro experiments, we observed that CCI treatment significantly upregulated DJ-1 expression and enhanced the colocalization of Atox1 and DJ-1 through immunofluorescence analysis (Suppl. Figs. 4B and C). Consistent with the immunofluorescence analysis, co-immunoprecipitation analysis revealed that CCI treatment enhances the interaction between Atox1 and DJ-1 in hippocampus (Suppl. Fig. 4D). To investigate whether the role of Atox1 in alleviating oxidative stress is dependent on DJ-1, we constructed HT-22 cells with knockdown of DJ-1. Out of the three tested DJ-1 interference sequences, one exhibited the highest efficacy in reducing DJ-1 expression (Suppl. Figs. 5A and B). Functionally, DJ-1 siRNA treatment attenuated the ability of Atox1 to reduce cellular and mitochondrial ROS levels, as indicated by increased ROS and MitoSOX fluorescence intensity (Fig. 8D–F). Superoxide dismutase (SOD) is a vital component of the antioxidant enzyme system in biological systems, playing a pivotal role in maintaining the balance between oxidation and antioxidation within the body. It facilitates the dismutation of superoxide anion free radicals into oxygen and hydrogen peroxide. Notably, copper and zinc ions are essential for the activities of SOD1 and SOD3 proteins within the SOD protein family [54,55]. Previous studies have reported that Cu chaperone Atox1 enhance SOD3, but not SOD1, activities by regulating copper ion transport and distribution [56,57]. Therefore, we proceeded to investigate the impact of Atox1 overexpression on mitigating oxidative stress in stretch-treated HT-22 cells. As shown in Fig. 8G, overexpression of Atox1 significantly augmented the activities of SOD1 and SOD3 in HT-22 cells subjected to stretch treatment. The knockdown of DJ-1 inhibited the activation of SOD1 by Atox1, without affecting the activation status of SOD3. Meanwhile, overexpression of Atox1 significantly upregulated the RNA and protein levels of SOD1 and SOD3, however, knockdown of DJ-1 affected the expression of SOD1, while the RNA and protein levels of SOD3 remained unaffected (Suppl. Figs. 5C and D). These results indicated that Atox1-DJ-1 axis modulates oxidative stress by selectively activating SOD1 rather than SOD3.

Based on previous research, DJ-1 facilitates mitophagy to promote cell survival and exert neuroprotective effects [37,58]. As shown in Fig. 8H, the upregulation of mitophagy-related protein induced by Atox1 is significantly attenuated upon transfection with si-DJ-1 in HT-22 cells treated with stretch. The immunofluorescence double-label staining assay demonstrated a significant reduction in the co-localization of mitochondria and autophagosome upon DJ-1 knockdown (Fig. 8I). Additionally, stretch-treated HT-22 cells overexpressing Atox1 exhibited improved mitochondrial structure and increased mitophagic vesicles (green arrowhead and white arrowhead), while DJ-1 knockdown attenuated the protective effect of Atox1 on mitochondria (red arrowhead) and impaired damaged mitochondria clearance (Fig. 8J). These results demonstrate that DJ-1 is required for the antioxidant stress response of Atox1.

3.8. Copper-binding motif is critical for the protective mechanism of Atox1

As CXXC and CXXXC motifs, where X represents any amino acid residue, are commonly recognized as copper-binding sites in metalloproteins [52], we generated an Atox1 construct ($Atox1^{12S15S}$) by substituting serine for cysteine residues at positions 12 and 15 to eliminate the copper-binding capacity of Atox1 [59]. To investigate the significance of the copper-binding site in the interaction between Atox1 and DJ-1, we conducted transfection experiments with overexpressed $Atox1^{WT}$ and $Atox1^{12S15S}$ variants, both of which were designed to incorporate carboxy-terminal FLAG sequences (Fig. 9A).

The immunoprecipitation analysis revealed that even under stretch stimulation, DJ-1 exhibited impaired binding to mutant variant $Atox1^{12S15S}$ (Fig. 9B), suggesting that the interaction between Atox1 and DJ-1 necessitates the involvement of a copper-binding site. The copper chelator TTM is utilized in clinical trials for the treatment of Wilson's disease. Due to its significant ability to reduce intracellular levels of copper ions, there is mounting evidence suggesting that copper chelator TTM holds potential for various other clinical applications. In this study,

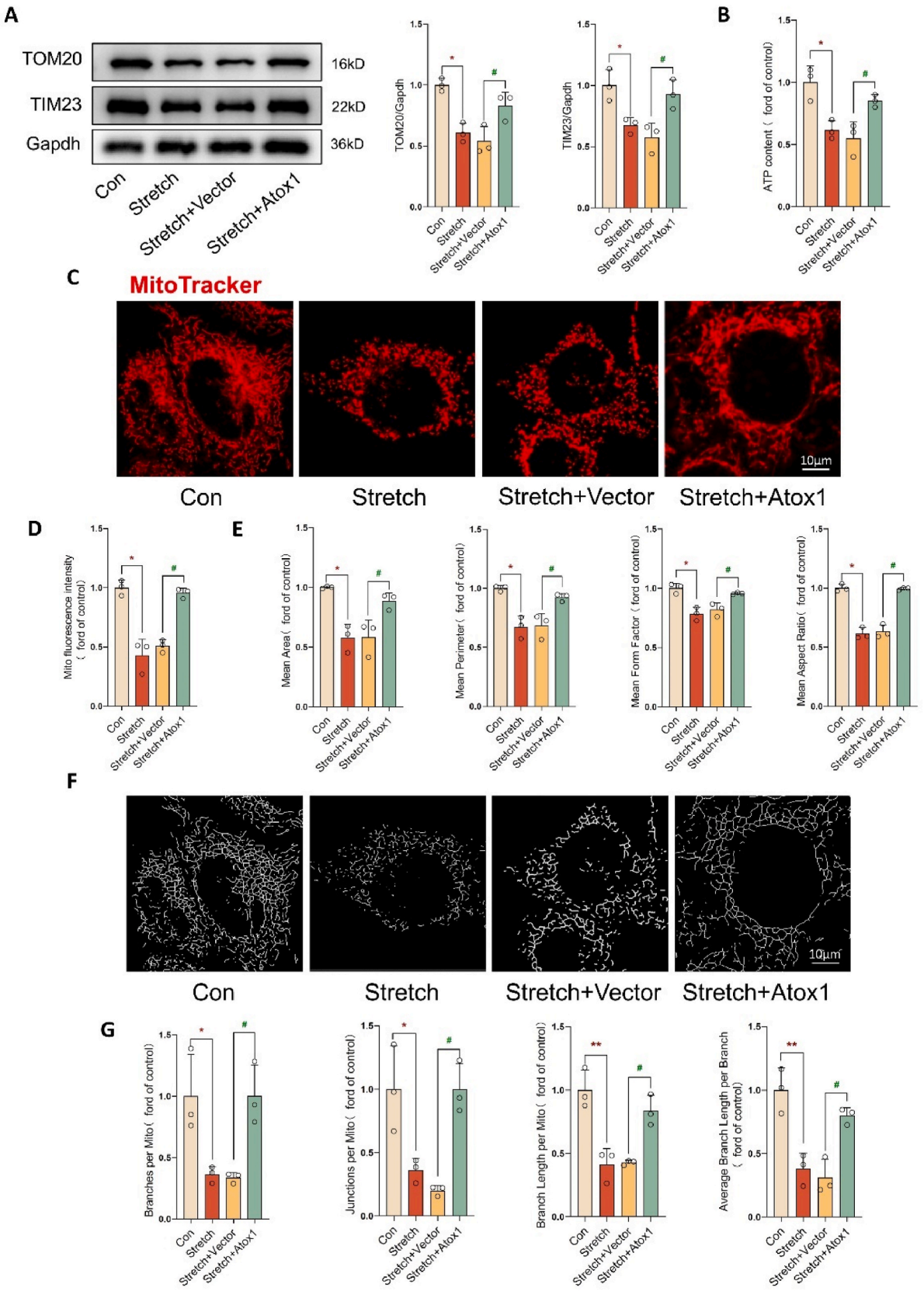

Fig. 5. Atox1 overexpression maintains mitochondrial structure after stretch treatment. (A) Western blot images of TOM20 and TIM23 in HT-22 cells, and the statistical results (n = 3). (B) The ATP level (n = 3). (C, D) Representative images of mitochondria labeled with red (Mito-Tracker Red CMXRos, MTR), and the statistical results (Scale bar is 10 μm, n = 3). (E) 2D morphological analysis of all cells in each group (n = 3). (F) Skeletonization of the mitochondrial objects identified in C (Scale bar is 10 μm, n = 3). (G) Quantitative analysis and comparison of mitochondrial network connectivity performed on all cells in each group (n = 3). Values represent the mean ± standard deviation (SD). *P < 0.05 vs. control group, **P < 0.01 vs. control group, #P < 0.05 vs. stretch + Vector group.

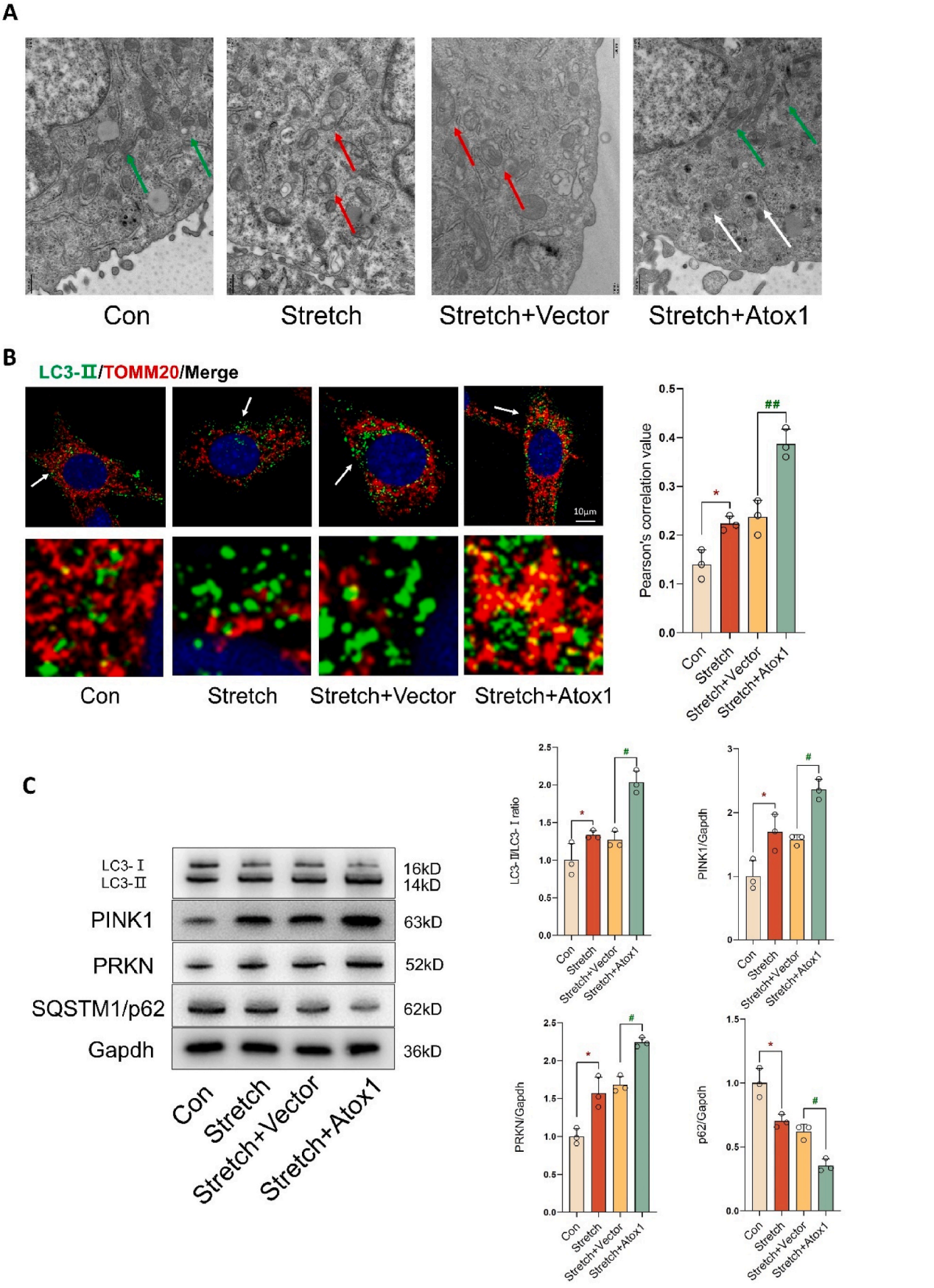

(caption on next page)

Fig. 6. Atox1 overexpression promotes mitophagy after stretch treatment. (A) Representative images of transmission electron microscopy (green arrow indicated the mitochondrion with intact structures and visible cristae, red arrow indicated the mitochondrion with aberrant morphology, and white arrow indicated isolated mitochondria in autophagosomes. Scale bar is 500 nm, n = 3). (B) Representative images of autolysosomes labeled with green (LC3-II) and mitochondria labeled with red (TOMM20) are utilized. Co-localization of both signals is quantified as a mitophagy event. Statistical analysis involves calculating the Pearson's coefficient for colocalization of LC3-II and TOMM20 (white arrow represents the zoom area. Scale bar is 10 μm, n = 3). (C) Western blot images of LC3, PINK1, PRKN and SQSTM1/p62 in HT-22 cells, and the statistical results (n = 3). Values represent the mean ± standard deviation (SD). *P < 0.05 vs. control group, #P < 0.05 vs. stretch + Vector group.

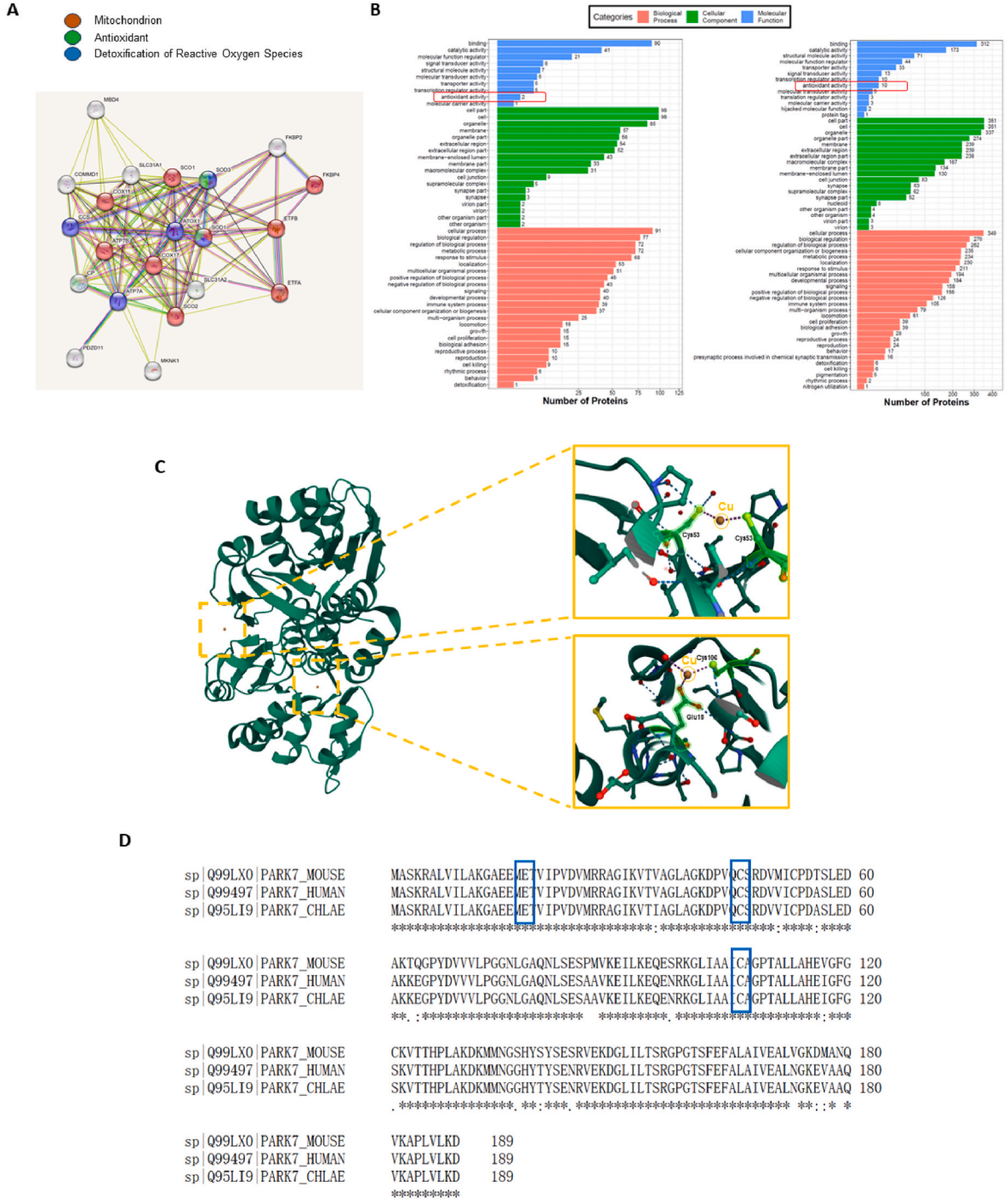

Fig. 7. Atox1 may interact with another copper-binding protein after injury. (A) Predicted interaction network for Atox1 and the confident hits based on String analysis. (B) GO enrichment analysis of the mass spectrometry data. (C) DJ-1 protein domains taken from the protein data bank (PDB DOI: https://doi.org/10.2210/pdb4mnt/pdb). Copper ions are shown as orange spheres. (D) Alignment of full-length amino acid sequences of DJ-1 proteins from different species, blue highlights indicate cysteine positions in DJ-1.

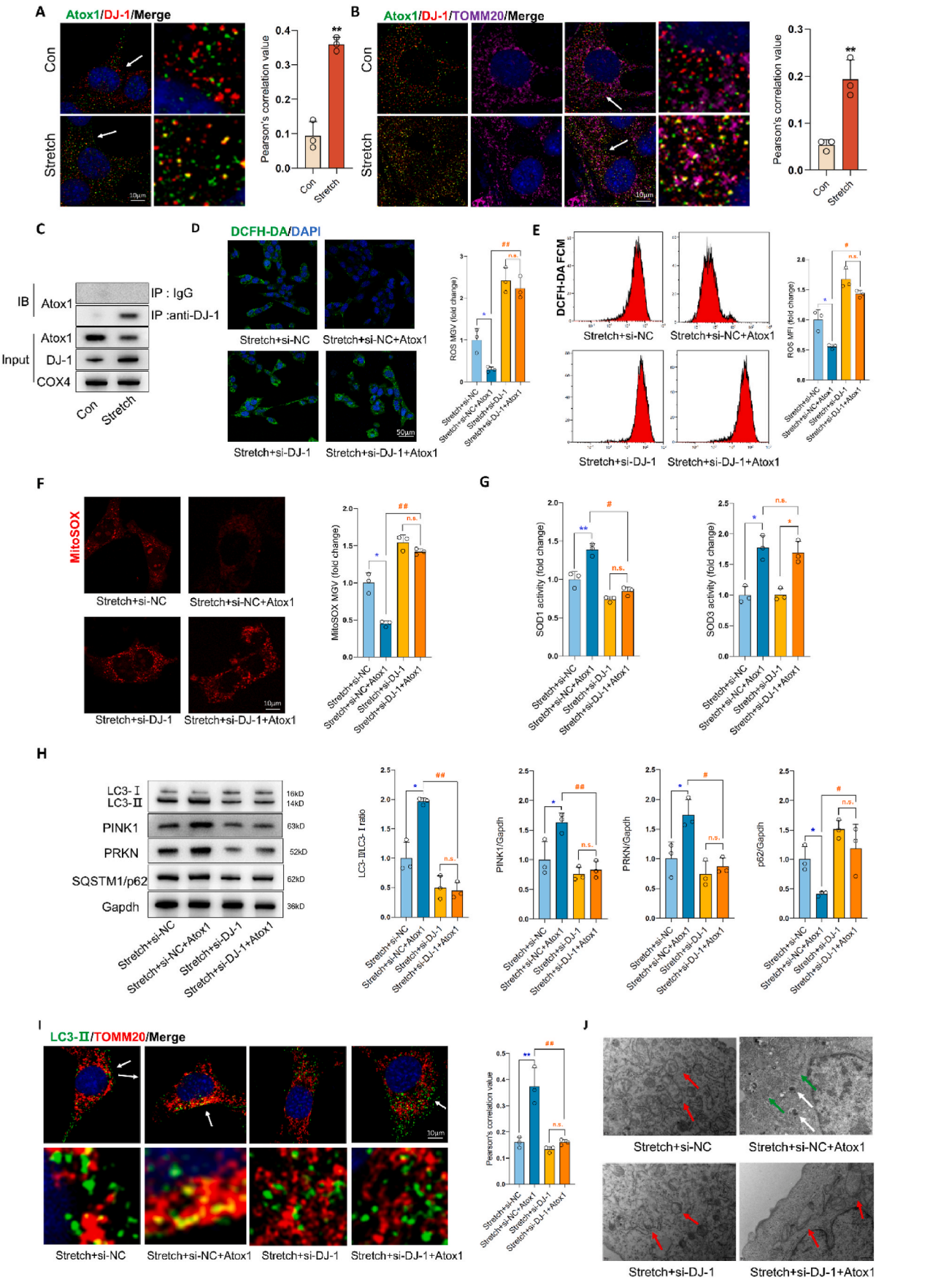

(caption on next page)

Fig. 8. Atox1 attenuates oxidative stress and promotes mitophagy via DJ-1. (A) Representative images of immunofluorescence staining of Atox1 (Green) and DJ-1 (Red) in HT-22 cells. Statistical analysis involves calculating the Pearson's coefficient for colocalization of green and red fluorescence intensities (white arrow represents the zoom area.Scale bar is 10 μm, n = 3). (B) Representative images of immunofluorescence staining of Atox1 (Green), DJ-1 (Red) and TOMM20 (purple) in HT-22 cells. Statistical analysis involves calculating the Pearson's coefficient for colocalization of green, red and purple fluorescence intensities (white arrow represents the zoom area. Scale bar is 10 μm, n = 3). (C) Representative images of co-immunoprecipitation of DJ-1 and Atox1 in mitochondria of HT-22 cells (n = 3). (D, E) Representative images and flow cytometric analysis of ROS level, and relative quantification. (Scale bar is 50 μm, n = 3). (F) Representative images of MitoSOX staining, and relative quantification. (Scale bar is 10 μm, n = 3). (G) The activity of SOD1 and SOD3 in HT-22 cells (n = 3). (H) Western blot images of LC3, PINK1, PRKN and SQSTM1/p62 in HT-22 cells, and the statistical results (n = 3). (I) Representative images of lysosomes labeled with green (LC3-II) and mitochondria labeled with r (TOMM20) are utilized. Co-localization of both signals is quantified as a mitophagy event. Statistical analysis involves calculating the Pearson's coefficient for colocalization of LC3-II and TOMM20 (white arrow represents the zoom area. Scale bar is 10 μm, n = 3). (J) Representative images of transmission electron microscopy (green arrow indicated the mitochondrion with intact structures and visible cristae, red arrow indicated the mitochondrion with aberrant morphology, and white arrow indicated isolated mitochondria in autophagosomes. Scale bar is 500 nm, n = 3). Values represent the mean ± standard deviation (SD). **(black) $P < 0.01$ vs. control group, *(blue) $P < 0.05$ vs. Stretch + siNC group, **(blue) $P < 0.01$ vs. Stretch + siNC group, *(orange) $P < 0.05$ vs. Stretch + si-DJ-1 group, #(orange) $P < 0.05$ vs. Stretch + si-DJ-1+Atox1 group, ##(orange) $P < 0.01$ vs. Stretch + si-DJ-1+Atox1 group, and n.s.: no significant difference.

we employed copper chelator TTM to eliminate free copper ions from the culture medium as a means to investigate the impact of copper ions on the interaction between Atox1 and DJ-1. The binding of $Atox1^{WT}$ to DJ-1 was significantly diminished upon removal of copper ions, as illustrated in Fig. 9C. Additionally, immunofluorescence staining also showed that the interaction between Atox1 and DJ-1 was affected in the presence of copper-binding motif mutation or copper depletion (Fig. 9D and E). The collective data indicate that the interaction between Atox1 and DJ-1 necessitates a copper-binding site as well as the presence of copper ion.

We subsequently investigated whether mutations in the copper-binding motif affected the cytoprotective effect of Atox1. The results from cell viability experiments demonstrated that overexpression of mutant variant $Atox1^{12S15S}$ failed to rescue stretch-treated HT-22 cells survival, even when DJ-1 was simultaneously overexpressed (Fig. 9F). Furthermore, overexpression of mutant variant $Atox1^{12S15S}$ did not exhibit a significant reduction in apoptotic percentages compared to those treated with wild-type Atox1 (Fig. 9G). Notably, we observed a substantial elevation in cleaved caspase-3 and Bax expression levels along with a decline in Bcl-2 levels in stretch-treated HT-22 cells, and these alterations remained largely unaffected after upregulating mutant variant $Atox1^{12S15S}$ even in the presence of enhanced DJ-1 expression (Fig. 9H).

Similarly, we conducted CCI modeling in mice following $Atox1^{12S15S}$ overexpression (Suppl. Fig. 6A), followed by behavioral experiments akin to those previously performed. However, the memory-related behavioral tests revealed that mice with $Atox1^{12S15S}$ overexpression still exhibited significant memory impairment compared to CCI-treated mice, without any notable improvement (Suppl. Fig. 6B-O). And, the overexpression of $Atox1^{12S15S}$ did not moderate mitochondrial swelling and outer membrane rupture after CCI (Suppl. Fig. 7A, red arrowhead). Additionally, CCI induced oxidative stress, as evidenced by decreased GSH levels and increased MDA and GSSG levels. LV- $Atox1^{12S15S}$ -pre-treated mice exhibited similar levels of oxidative stress (Suppl. Fig. 7B). These data suggest that the presence of copper-binding sites is crucial for proper functioning of Atox1.

We also used histological (TUNEL assay, hippocampus neurons), molecular (anti-oxidant enzyme capacity, oxidative damage) and behavioral experiments to assess the function of copper chelator TTM, which TTM (0.7 mg/d, oral gavage) was administered to mice one week before CCI [60]. Unexpectedly, administration with copper chelator TTM failed to reduce the proportion of apoptotic neurons or the level of oxidative stress in hippocampal region of mice with CCI (Suppl. Figs. 8A–D). Furthermore, behavioral tests revealed that TTM-treated mice did not exhibit improved learning and memory abilities (Suppl. Fig. 9A-N). These findings suggest that oral administration of copper chelator TTM does not ameliorate the pathological processes associated with CCI.

4. Discussion

TBI is a mechanical insult that immediately causes damage at the site of impact due to direct trauma. Currently, surgical intervention remains the primary treatment approach for severe TBI in clinical practice; however, limited progress has been made in developing pharmacological therapies aimed at inhibiting cell death induced by secondary injury and subsequent lesion propagation [4,61]. This lack of advancement holds significant implications for enhancing the prognosis and quality of life among TBI patients. The present study elucidated the neuroprotective role of Atox1 in the pathophysiology following CCI. Based on these research findings, we demonstrated a significant reduction in the expression level of Atox1 specifically within the hippocampal region of mice after CCI at 6 h, 24 h, and 3 days, while no evident changes were observed in the cortical region. Furthermore, our results highlight that upregulation of Atox1 expression within the hippocampus plays a crucial role in mitigating neuronal apoptosis and ameliorating deficits in memory-related behavioral abilities. Mechanistically, we have identified Atox1 has antioxidant properties following trauma, which enhances neuronal health by reducing levels of ROS and promoting mitophagy. We further demonstrated a close association between DJ-1 and the neuroprotective function, whereby the absence of DJ-1 not only hindered the antioxidant properties of Atox1 but also diminished mitophagy levels in Atox1-overexpressing neurons. Furthermore, we observed that mutation of the copper-binding motif impaired the interaction between Atox1 and DJ-1. The present study offers a systematic elucidation of the role played by Atox1 in CCI, unveiling its potential mechanism and presenting promising therapeutic strategies for managing patients with neurological dysfunction in clinical practice.

Oxidative stress is characterized by the excessive production of oxygen free radicals and other reactive oxygen species in both intracellular and extracellular environments, resulting in an imbalance of redox [62]. In the context of traumatic brain injury, oxidative stress can induce lipid peroxidation of cell membranes, oxidative damage to DNA and proteins, as well as activate inflammatory responses [7,63]. Studies have demonstrated that the interaction between copper ions and mitochondrial oxidative stress encompasses multiple facets. Firstly, free copper ions can participate in intracellular REDOX reactions, resulting in the generation of highly ROS such as superoxide anion, hydroperoxides, and hydroxyl radicals. These ROS exhibit strong chemical activity and can undergo oxidative reactions with intracellular biological macromolecules including lipids, proteins, and nucleic acids, leading to cellular damage and increased oxidative stress [64–66]. Secondly, free copper ions can act as catalysts for lipid peroxidation reaction which results in the peroxidation of cell membrane lipids. The resultant free radicals from lipid peroxidation initiate a chain reaction that induces structural and functional alterations in cell membranes thereby affecting normal nervous system function [67,68]. In the present study, we observed a significant reduction in Atox1, an essential copper chaperone protein, within the hippocampus of CCI mice. Considering the crucial role of Atox1 in copper ion uptake, transport, and delivery, our hypothesis

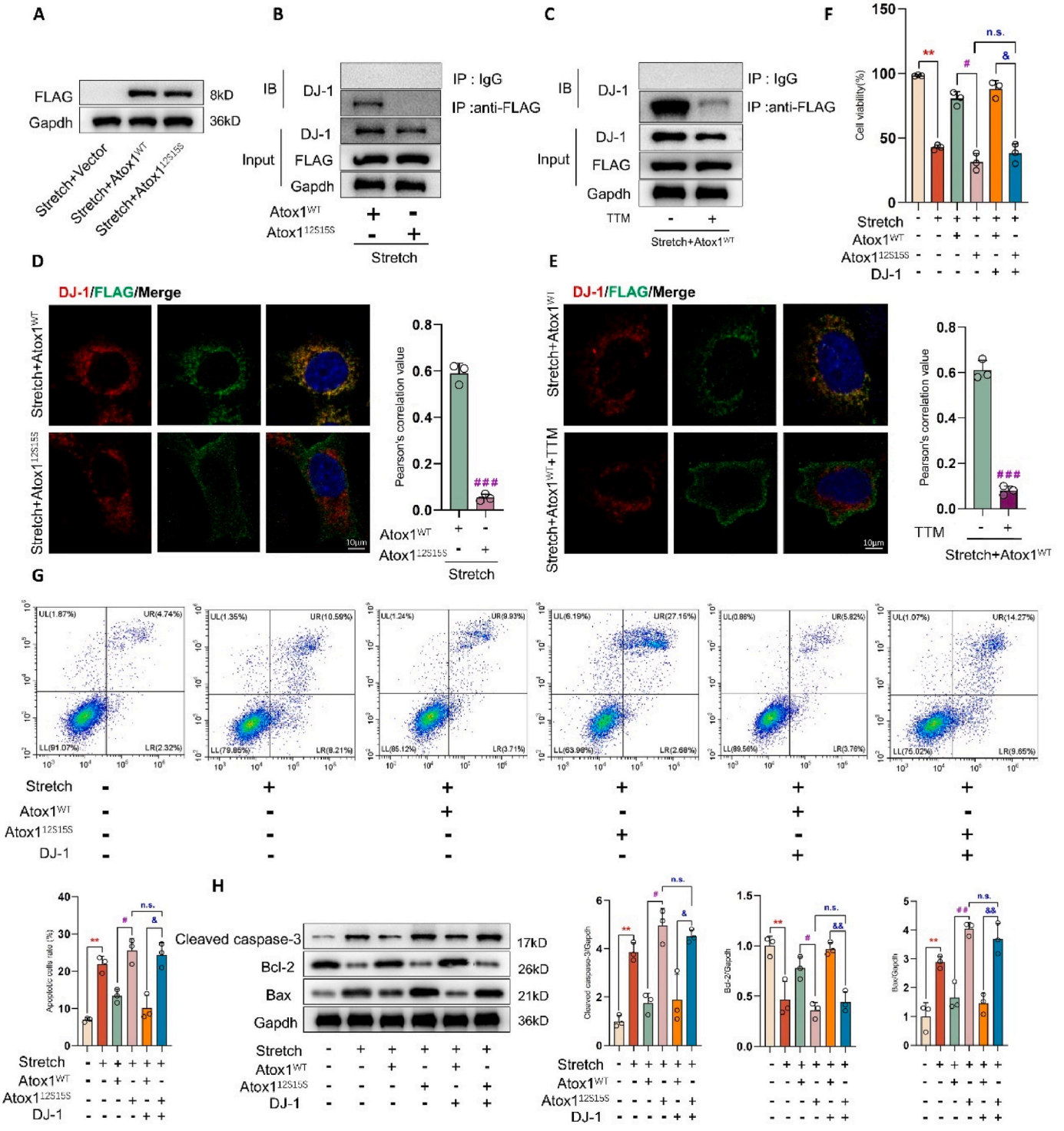

Fig. 9. Copper binding motif is critical for the protective mechanism of Atox1. (A) Western blot images of FLAG in HT-22 cells (n = 3). (B, C) Representative images of co-immunoprecipitation of DJ-1 and FLAG in HT-22 cells (n = 3). (D, E) Representative images of immunofluorescence staining of Atox1 (Green) and DJ-1 (Red) in HT-22 cells. Statistical analysis involves calculating the Pearson's coefficient for colocalization of gree and red fluorescence intensities (Scale bar is 10 μm, n = 3). (F) Cell viability detected via CCK-8 assay kit (n = 3). (G) Cell apoptosis rate was determined using flow cytometry (n = 3). (H) Western blot images of Cleaved caspase-3, Bcl-2 and Bax in hippocampus region, and the statistical results (n = 3). Values represent the mean ± standard deviation (SD). **P < 0.01 vs. control group, #P < 0.05 vs. Stretch + Atox1^{WT} group, ##P < 0.01 vs. Stretch + Atox1^{WT} group, ###P < 0.001 vs. Stretch + Atox1^{WT} group, &P < 0.05 vs. Stretch + Atox1^{WT} + DJ-1 group, &&P < 0.01 vs. Stretch + Atox1^{WT} + DJ-1 group, and n.s.: no significant difference.

suggests that alterations in Atox1 content may contribute to increased levels of free copper ions following CCI. Therefore, the objective of this study was to investigate the potential role of Atox1 in the neuroprotective effect following CCI, as well as the underlying mechanisms.

The current research on Atox1 primarily focuses on its role in intracellular copper ion transport and regulation of oxidative stress, as it is a protein capable of binding to copper ions. Recent studies have demonstrated the anti-apoptotic function of Atox1 in cerebral ischemic

and neurodegenerative diseases [31]. Additionally, modification of the copper-binding domain in Atox1 abolishes its antioxidative stress activity [59]. Therefore, investigating whether Atox1 can mitigate neuronal apoptosis and oxidative stress is crucial for understanding the complex pathophysiological processes following TBI. In the CCI model, we observed a significant reduction in neuronal apoptosis rate and oxidative stress level in the hippocampal region upon Atox1 overexpression. The hippocampus, being a crucial brain structure, serves as a pivotal region for memory and learning processes. It plays a significant role in spatial memory, factual memory, and episodic memory [49]. Impairment of hippocampal function resulting from injury or lesion can profoundly impact both memory and learning abilities. Henceforth, considering the neuroprotective effects of Atox1 against neuronal apoptosis and oxidative stress observed in the CCI model, we proceeded to assess the impact of Atox1 on neurological function following CCI. The results of our study demonstrate that the overexpression of Atox1 effectively mitigated both short-term and long-term memory impairment in mice with CCI. Additionally, by conducting quantitative analysis on mitochondrial morphology and network characteristics [51], we observed a significant reduction in mid-fragmented mitochondria and the preservation of mitochondrial network integrity in mechanically stretched HT-22 cells upon Atox1 overexpression. Furthermore, our findings indicate that Atox1 promotes mitophagy, suggesting its role in mitigating oxidative stress through facilitating the removal of damaged mitochondria.

It is widely recognized that copper ion transportation represents a crucial attribute of Atox1 [18,22]. Previous studies have demonstrated the loss of neuroprotective efficacy in mutated forms of Atox1's copper-binding domain [59]. Atox1 facilitates the translocation of copper ions to the nuclear copper binding protein CRIP2, thereby inducing alterations in its secondary structure and promoting ubiquitin-mediated proteasomal degradation [22]. Moreover, Atox1 orchestrates breast cancer cell migration through co-transportation of copper ions on the ATP7A-LOX axis [69]. However, the precise molecular mechanism underlying its transfer function in craniocerebral traumatic disease remains elusive. To gain a deeper understanding of the relationship between Atox1 and the pathological process of TBI, we utilized a combination of co-immunoprecipitation assay and mass spectrometry analysis to characterize the proteins that interact with Atox1 following TBI. Through this method, we successfully identified DJ-1 as an interacting protein with Atox1 that functions as a copper-binding protein. Literatures have demonstrated that DJ-1 is a type of metal-binding protein involved in the regulation of metal homeostasis, which can protect cells from induced metal toxicity [40]. Additionally, in neurodegenerative diseases, DJ-1 increases SOD1 activity through copper binding to provide resistance against oxidative stress [41]. In our experiments, we confirmed that the interaction between Atox1 and DJ-1 is more pronounced under conditions of cellular injury. Furthermore, it has been demonstrated that DJ-1 plays a crucial role in mediating the cytoprotective function of Atox1. We similarly conducted an investigation to determine the criticality of the copper binding site for DJ-1 in mediating Atox1 protein function. Our findings revealed that either mutating the copper binding site of Atox1 or removing free copper ions from the culture medium resulted in the loss of Atox1's ability to bind to DJ-1. Furthermore, mutant $Atox1^{12S15S}$ exhibited an inability to exert neuroprotective functions. Similarly, we investigated the neuroprotective effect of a copper chelator TTM following CCI and observed no significant reduction in the proportion of neuronal apoptosis or oxidative stress levels after CCI when administered alone. Furthermore, it did not demonstrate any impact on neurological function related to learning and memory. In conclusion, we investigated the role of Atox1 in neuronal response to mechanical injury and discovered that Atox1 exerts its protective ability against oxidative stress and facilitates damaged mitochondria removal in a DJ-1-dependent manner. Furthermore, the interaction between Atox1 and DJ-1 relies on copper ion delivery. However, the use of gene therapy in human TBI is limited due to its unpredictable occurrence. Furthermore, without additional clinical studies, it is difficult to assess the relevance of our findings to the in vivo situation in TBI patients. Nevertheless, recent research has demonstrated that targeting metallochaperones presents a promising therapeutic approach following injury. Our study also uncovers a potential neuroprotective target that enhances understanding of the metal delivery process and its role in the pathological progression of TBI.

Funding

This study was supported by grants from National Natural Science Foundation of China (Grant No. 82120108018), National Key Research and Development Program of China (Grant No. 2021YFA1101802-2), and Gusu School, Nanjing Medical University (Grant No. GSKY202201010).

Availability of data and materials

The raw data supporting the conclusions of this article are available from the corresponding author upon reasonable request.

CRediT authorship contribution statement

Pengzhan Zhao: Writing – review & editing, Writing – original draft, Visualization, Software, Project administration, Data curation. **Wenqian Shi:** Software, Methodology. **Yangfan Ye:** Software, Data curation. **Ke Xu:** Methodology. **Jingming Hu:** Formal analysis, Software. **Honglu Chao:** Software, Validation. **ZeQiang Tao:** Validation. **Lei Xu:** Project administration. **Wei Gu:** Software. **Liuchao Zhang:** Investigation. **Tian Wang:** Formal analysis. **Xinyue Wang:** Methodology. **Jing Ji:** Writing – review & editing, Supervision, Funding acquisition, Conceptualization.

Declaration of competing interest

The authors declare that the research was conducted in the absence of any commercial or financial relationships that could be construed as a potential conflict of interest.

Data availability

Data will be made available on request.

Acknowledgments

The authors wish to thank Jiangsu Province Hospital Core Facility Center for providing experimental platform.

Abbreviations

TBI	Traumatic brain injury
CCI	Controlled cortical impact
MWM	Morris water maze
MOI	Multiplicity of infection
TUNEL	Terminal deoxynucleotidyl transferase mediated dUTP nick end labeling
ROS	Reactive oxygen species
TEM	Transmission electron microscopy
MFI	Mean fluorescence intensity
MGV	mean grey values
MDA	malondialdehyde
CNS	central nervous system
FF	form factor
AR	aspect ratio
TTM	ammonium tetrathiomolybdate
SOD	superoxide dismutase

Appendix A. Supplementary data

Supplementary data to this article can be found online at https://doi.org/10.1016/j.redox.2024.103156.

References

[1] N. Andelic, The epidemiology of traumatic brain injury, Lancet Neurol. 12 (1) (2013) 28–29, https://doi.org/10.1016/S1474-4422(12)70294-6.

[2] A.I.R. Maas, D.K. Menon, P.D. Adelson, N. Andelic, M.J. Bell, A. Belli, P. Bragge, A. Brazinova, A. Buki, R.M. Chesnut, et al., Traumatic brain injury: integrated approaches to improve prevention, clinical care, and research, Lancet Neurol. 16 (12) (2017) 987–1048, https://doi.org/10.1016/S1474-4422(17)30371-X.

[3] J.A. Prvu-Bettger, B.E. Bates, D.E. Bidelspach, M.G. Stineman, Short- and long-term prognosis among veterans with neurological disorders and subsequent lower-extremity amputation, Neuroepidemiology 32 (1) (2009) 4–10, https://doi.org/10.1159/000170085.

[4] N. Stocchetti, M. Carbonara, G. Citerio, A. Ercole, M.B. Skrifvars, P. Smielewski, T. Zoerle, D.K. Menon, Severe traumatic brain injury: targeted management in the intensive care unit, Lancet Neurol. 16 (6) (2017) 452–464, https://doi.org/10.1016/S1474-4422(17)30118-7.

[5] L. Wilson, W. Stewart, K. Dams-O'Connor, R. Diaz-Arrastia, L. Horton, D.K. Menon, S. Polinder, The chronic and evolving neurological consequences of traumatic brain injury, Lancet Neurol. 16 (10) (2017) 813–825, https://doi.org/10.1016/S1474-4422(17)30279-X.

[6] G.C. Brown, A. Vilalta, M. Fricker, Phagoptosis - cell death by phagocytosis - plays central roles in physiology, host defense and pathology, Curr. Mol. Med. 15 (9) (2015) 842–851, https://doi.org/10.2174/1566524015091511051306 28.

[7] H. Chao, T.S. Anthonymuthu, E.M. Kenny, A.A. Amoscato, L.K. Cole, G.M. Hatch, J. Ji, V.E. Kagan, H. Bayir, Disentangling oxidation/hydrolysis reactions of brain mitochondrial cardiolipins in pathogenesis of traumatic injury, JCI Insight 3 (21) (2018), https://doi.org/10.1172/jci.insight.97677.

[8] J. Ji, Y.Y. Tyurina, M. Tang, W. Feng, D.B. Stolz, R.S. Clark, D.F. Meaney, P. M. Kochanek, V.E. Kagan, H. Bayir, Mitochondrial injury after mechanical stretch of cortical neurons in vitro: biomarkers of apoptosis and selective peroxidation of anionic phospholipids, J. Neurotrauma 29 (5) (2012) 776–788, https://doi.org/10.1089/neu.2010.1602.

[9] W. Cui, X. Wu, Y. Shi, W. Guo, J. Luo, H. Liu, L. Zheng, Y. Du, P. Wang, Q. Wang, et al., 20-HETE synthesis inhibition attenuates traumatic brain injury-induced mitochondrial dysfunction and neuronal apoptosis via the SIRT1/PGC-1alpha pathway: a translational study, Cell Prolif. 54 (2) (2021) e12964, https://doi.org/10.1111/cpr.12964.

[10] W. Xie, D. Guo, J. Li, L. Yue, Q. Kang, G. Chen, T. Zhou, H. Wang, K. Zhuang, L. Leng, et al., CEND1 deficiency induces mitochondrial dysfunction and cognitive impairment in Alzheimer's disease, Cell Death Differ. 29 (12) (2022) 2417–2428, https://doi.org/10.1038/s41418-022-01027-7.

[11] L. La Barbera, A. Nobili, E. Cauzzi, I. Paoletti, M. Federici, L. Saba, C. Giacomet, R. Marino, P. Krashia, M. Melone, et al., Upregulation of Ca(2+)-binding proteins contributes to VTA dopamine neuron survival in the early phases of Alzheimer's disease in Tg2576 mice, Mol. Neurodegener. 17 (1) (2022) 76, https://doi.org/10.1186/s13024-022-00580-6.

[12] J.D. Pandya, S. Musyaju, H.R. Modi, Y. Cao, W.J. Flerlage, L. Huynh, B. Kociuba, N. P. Visavadiya, F. Kobeissy, K. Wang, et al., Comprehensive evaluation of mitochondrial redox profile, calcium dynamics, membrane integrity and apoptosis markers in a preclinical model of severe penetrating traumatic brain injury, Free Radic. Biol. Med. 198 (2023) 44–58, https://doi.org/10.1016/j.freeradbiomed.2023.02.001.

[13] J. Rihel, Copper on the brain, Nat. Chem. Biol. 14 (7) (2018) 638–639, https://doi.org/10.1038/s41589-018-0089-1.

[14] J. Garcia-Panach, N. Lull, J.J. Lull, J. Ferri, C. Martinez, P. Sopena, M. Robles, J. Chirivella, E. Noe, A voxel-based analysis of FDG-PET in traumatic brain injury: regional metabolism and relationship between the thalamus and cortical areas, J. Neurotrauma 28 (9) (2011) 1707–1717, https://doi.org/10.1089/neu.2011.1851.

[15] S. Lutsenko, A. Bhattacharjee, A.L. Hubbard, Copper handling machinery of the brain, Metallomics 2 (9) (2010) 596–608, https://doi.org/10.1039/c0mt00006j.

[16] G. Gupta, F. Cappellini, L. Farcal, R. Gornati, G. Bernardini, B. Fadeel, Copper oxide nanoparticles trigger macrophage cell death with misfolding of Cu/Zn superoxide dismutase 1 (SOD1), Part. Fibre Toxicol. 19 (1) (2022) 33, https://doi.org/10.1186/s12989-022-00467-w.

[17] A. Lewen, T. Sugawara, Y. Gasche, M. Fujimura, P.H. Chan, Oxidative cellular damage and the reduction of APE/Ref-1 expression after experimental traumatic brain injury, Neurobiol. Dis. 8 (3) (2001) 380–390, https://doi.org/10.1006/nbdi.2001.0396.

[18] Q. Xue, R. Kang, D.J. Klionsky, D. Tang, J. Liu, X. Chen, Copper metabolism in cell death and autophagy, Autophagy 19 (8) (2023) 2175–2195, https://doi.org/10.1080/15548627.2023.2200554.

[19] A.V. Gyulkhandanyan, C.J. Feeney, P.S. Pennefather, Modulation of mitochondrial membrane potential and reactive oxygen species production by copper in astrocytes, J. Neurochem. 87 (2) (2003) 448–460, https://doi.org/10.1046/j.1471-4159.2003.02029.x.

[20] Y. Li, H. Chen, J. Liao, K. Chen, M.T. Javed, N. Qiao, Q. Zeng, B. Liu, J. Yi, Z. Tang, et al., Long-term copper exposure promotes apoptosis and autophagy by inducing oxidative stress in pig testis, Environ. Sci. Pollut. Res. Int. 28 (39) (2021) 55140–55153, https://doi.org/10.1007/s11356-021-14853-y.

[21] D. Natera-de Benito, A. Sola, P.R. Sousa, S. Boronat, J. Exposito-Escudero, L. Carrera-Garcia, C. Ortez, C. Jou, J. Muchart, M. Rebollo, et al., Copper toxicity associated with an atp7a-related complex phenotype, Pediatr. Neurol. 119 (2021) 40–44, https://doi.org/10.1016/j.pediatrneurol.2021.03.005.

[22] L. Chen, N. Li, M. Zhang, M. Sun, J. Bian, B. Yang, Z. Li, J. Wang, F. Li, X. Shi, et al., APEX2-based proximity labeling of Atox1 identifies CRIP2 as a nuclear copper-binding protein that regulates autophagy activation, Angew Chem. Int. Ed. Engl. 60 (48) (2021) 25346–25355, https://doi.org/10.1002/anie.202108961.

[23] N.K. Isaev, E.V. Stelmashook, E.E. Genrikhs, Role of zinc and copper ions in the pathogenetic mechanisms of traumatic brain injury and Alzheimer's disease, Rev. Neurosci. 31 (3) (2020) 233–243, https://doi.org/10.1515/revneuro-2019-0052.

[24] A. Vitaliti, A. De Luca, L. Rossi, Copper-dependent kinases and their role in cancer inception, progression and metastasis, Biomolecules 12 (10) (2022), https://doi.org/10.3390/biom12101520.

[25] K. Chakraborty, S. Kar, B. Rai, R. Bhagat, N. Naskar, P. Seth, A. Gupta, A. Bhattacharjee, Copper dependent ERK1/2 phosphorylation is essential for the viability of neurons and not glia, Metallomics 14 (4) (2022), https://doi.org/10.1093/mtomcs/mfac005.

[26] J. Lee, M.J. Petris, D.J. Thiele, Characterization of mouse embryonic cells deficient in the ctr1 high affinity copper transporter. Identification of a Ctr1-independent copper transport system, J. Biol. Chem. 277 (43) (2002) 40253–40259, https://doi.org/10.1074/jbc.M208002200.

[27] I.F. Scheiber, J.F. Mercer, R. Dringen, Metabolism and functions of copper in brain, Prog. Neurobiol. 116 (2014) 33–57, https://doi.org/10.1016/j.pneurobio.2014.01.002.

[28] Y. An, S. Li, X. Huang, X. Chen, H. Shan, M. Zhang, The role of copper homeostasis in brain disease, Int. J. Mol. Sci. 23 (22) (2022), https://doi.org/10.3390/ijms232213850.

[29] C. White, T. Kambe, Y.G. Fulcher, S.W. Sachdev, A.I. Bush, K. Fritsche, J. Lee, T. P. Quinn, M.J. Petris, Copper transport into the secretory pathway is regulated by oxygen in macrophages, J. Cell Sci. 122 (Pt 9) (2009) 1315–1321, https://doi.org/10.1242/jcs.043216.

[30] Y. Hatori, S. Lutsenko, The role of copper chaperone Atox1 in coupling redox homeostasis to intracellular copper distribution, Antioxidants 5 (3) (2016), https://doi.org/10.3390/antiox5030025.

[31] S.M. Kim, I.K. Hwang, D.Y. Yoo, W.S. Eum, D.W. Kim, M.J. Shin, E.H. Ahn, H.S. Jo, E.J. Ryu, J.I. Yong, et al., Tat-antioxidant 1 protects against stress-induced hippocampal HT-22 cells death and attenuate ischaemic insult in animal model, J. Cell Mol. Med. 19 (6) (2015) 1333–1345, https://doi.org/10.1111/jcmm.12513.

[32] W.S. Eum, M.J. Shin, C.H. Lee, H.J. Yeo, E.J. Yeo, Y.J. Choi, H.J. Kwon, D.S. Kim, O.S. Kwon, K.W. Lee, et al., Neuroprotective effects of Tat-ATOX1 protein against MPP(+)-induced SH-SY5Y cell deaths and in MPTP-induced mouse model of Parkinson's disease, Biochimie 156 (2019) 158–168, https://doi.org/10.1016/j.biochi.2018.10.010.

[33] S. Montes, S. Rivera-Mancia, A. Diaz-Ruiz, L. Tristan-Lopez, C. Rios, Copper and copper proteins in Parkinson's disease, Oxid. Med. Cell. Longev. 2014 (2014) 147251, https://doi.org/10.1155/2014/147251.

[34] L.P. Dolgacheva, A.V. Berezhnov, E.I. Fedotova, V.P. Zinchenko, A.Y. Abramov, Role of DJ-1 in the mechanism of pathogenesis of Parkinson's disease, J. Bioenerg. Biomembr. 51 (3) (2019) 175–188, https://doi.org/10.1007/s10863-019-09798-4.

[35] H. Ariga, K. Takahashi-Niki, I. Kato, H. Maita, T. Niki, S.M. Iguchi-Ariga, Neuroprotective function of DJ-1 in Parkinson's disease, Oxid. Med. Cell. Longev. 2013 (2013) 683920, https://doi.org/10.1155/2013/683920.

[36] S.E. Oh, M.M. Mouradian, Cytoprotective mechanisms of DJ-1 against oxidative stress through modulating ERK1/2 and ASK1 signal transduction, Redox Biol. 14 (2018) 211–217, https://doi.org/10.1016/j.redox.2017.09.008.

[37] D. Imberechts, I. Kinnart, F. Wauters, J. Terbeek, L. Manders, K. Wierda, K. Eggermont, R.F. Madeiro, C. Sue, C. Verfaillie, et al., DJ-1 is an essential downstream mediator in PINK1/parkin-dependent mitophagy, Brain 145 (12) (2022) 4368–4384, https://doi.org/10.1093/brain/awac313.

[38] T. Wang, Y. Xue, Y. Li, S. Gao, L. Peng, Y. Zhao, S. Yu, DJ-1 protein inhibits apoptosis in cerebral ischemia by regulating the Notch1 and nuclear factor erythroid2-related factor 2 signaling pathways, Neuroscience 504 (2022) 33–46, https://doi.org/10.1016/j.neuroscience.2022.09.016.

[39] M. Mihoub, J. Abdallah, G. Richarme, Protein repair from glycation by glyoxals by the DJ-1 family maillard deglycases, Adv. Exp. Med. Biol. 1037 (2017) 133–147, https://doi.org/10.1007/978-981-10-6583-5_9.

[40] B. Bjorkblom, A. Adilbayeva, J. Maple-Grodem, D. Piston, M. Okvist, X.M. Xu, C. Brede, J.P. Larsen, S.G. Moller, Parkinson disease protein DJ-1 binds metals and protects against metal-induced cytotoxicity, J. Biol. Chem. 288 (31) (2013) 22809–22820, https://doi.org/10.1074/jbc.M113.482091.

[41] S. Girotto, L. Cendron, M. Bisaglia, I. Tessari, S. Mammi, G. Zanotti, L. Bubacco, DJ-1 is a copper chaperone acting on SOD1 activation, J. Biol. Chem. 289 (15) (2014) 10887–10899, https://doi.org/10.1074/jbc.M113.535112.

[42] Z. Bao, Y. Liu, B. Chen, Z. Miao, Y. Tu, C. Li, H. Chao, Y. Ye, X. Xu, G. Sun, et al., Prokineticin-2 prevents neuronal cell deaths in a model of traumatic brain injury, Nat. Commun. 12 (1) (2021) 4220, https://doi.org/10.1038/s41467-021-24469-y.

[43] N. Carty, D. Lee, C. Dickey, C. Ceballos-Diaz, K. Jansen-West, T.E. Golde, M. N. Gordon, D. Morgan, K. Nash, Convection-enhanced delivery and systemic mannitol increase gene product distribution of AAV vectors 5, 8, and 9 and increase gene product in the adult mouse brain, J. Neurosci. Methods 194 (1) (2010) 144–153, https://doi.org/10.1016/j.jneumeth.2010.10.010.

[44] E.E. Irvine, J. Vernon, K.P. Giese, AlphaCaMKII autophosphorylation contributes to rapid learning but is not necessary for memory, Nat. Neurosci. 8 (4) (2005) 411–412, https://doi.org/10.1038/nn1431.
[45] P. Zhao, Y. Wei, G. Sun, L. Xu, T. Wang, Y. Tian, H. Chao, Y. Tu, J. Ji, Fetuin-A alleviates neuroinflammation against traumatic brain injury-induced microglial necroptosis by regulating Nrf-2/HO-1 pathway, J. Neuroinflammation 19 (1) (2022) 269, https://doi.org/10.1186/s12974-022-02633-5.
[46] Y. Deng-Bryant, I.N. Singh, K.M. Carrico, E.D. Hall, Neuroprotective effects of tempol, a catalytic scavenger of peroxynitrite-derived free radicals, in a mouse traumatic brain injury model, J. Cerebr. Blood Flow Metabol. 28 (6) (2008) 1114–1126, https://doi.org/10.1038/jcbfm.2008.10.
[47] Z. Bao, L. Fan, L. Zhao, X. Xu, Y. Liu, H. Chao, N. Liu, Y. You, Y. Liu, X. Wang, et al., Silencing of A20 aggravates neuronal death and inflammation after traumatic brain injury: a potential trigger of necroptosis, Front. Mol. Neurosci. 12 (2019) 222, https://doi.org/10.3389/fnmol.2019.00222.
[48] S.D. Portbury, D.J. Hare, C. Sgambelloni, D.I. Finkelstein, P.A. Adlard, A time-course analysis of changes in cerebral metal levels following a controlled cortical impact, Metallomics 8 (2) (2016) 193–200, https://doi.org/10.1039/c5mt00234f.
[49] T. Bartsch, P. Wulff, The hippocampus in aging and disease: from plasticity to vulnerability, Neuroscience 309 (2015) 1–16, https://doi.org/10.1016/j.neuroscience.2015.07.084.
[50] Y. Shen, L. Hua, C.K. Yeh, L. Shen, M. Ying, Z. Zhang, G. Liu, S. Li, S. Chen, X. Chen, et al., Ultrasound with microbubbles improves memory, ameliorates pathology and modulates hippocampal proteomic changes in a triple transgenic mouse model of Alzheimer's disease, Theranostics 10 (25) (2020) 11794–11819, https://doi.org/10.7150/thno.44152.
[51] A. Chaudhry, R. Shi, D.S. Luciani, A pipeline for multidimensional confocal analysis of mitochondrial morphology, function, and dynamics in pancreatic beta-cells, Am. J. Physiol. Endocrinol. Metab. 318 (2) (2020) E87–E101, https://doi.org/10.1152/ajpendo.00457.2019.
[52] C.H. Yu, N. Yang, J. Bothe, M. Tonelli, S. Nokhrin, N.V. Dolgova, L. Braiterman, S. Lutsenko, O.Y. Dmitriev, The metal chaperone Atox1 regulates the activity of the human copper transporter ATP7B by modulating domain dynamics, J. Biol. Chem. 292 (44) (2017) 18169–18177, https://doi.org/10.1074/jbc.M117.811752.
[53] M.R. Puno, N.A. Patel, S.G. Moller, C.V. Robinson, P.C. Moody, M. Odell, Structure of Cu(I)-bound DJ-1 reveals a biscysteinate metal binding site at the homodimer interface: insights into mutational inactivation of DJ-1 in Parkinsonism, J. Am. Chem. Soc. 135 (43) (2013) 15974–15977, https://doi.org/10.1021/ja406010m.
[54] R. Dioszegi, D. Bonczidai-Kelemen, A.C. Benyei, N.V. May, I. Fabian, N. Lihi, Copper(II) complexes of pyridine-2,6-dicarboxamide ligands with high SOD activity, Inorg. Chem. 61 (4) (2022) 2319–2332, https://doi.org/10.1021/acs.inorgchem.1c03728.
[55] D.D. Wu, S. Jin, R.X. Cheng, W.J. Cai, W.L. Xue, Q.Q. Zhang, L.J. Yang, Q. Zhu, M. Y. Li, G. Lin, et al., Hydrogen sulfide functions as a micro-modulator bound at the copper active site of Cu/Zn-SOD to regulate the catalytic activity of the enzyme, Cell Rep. 42 (7) (2023) 112750, https://doi.org/10.1016/j.celrep.2023.112750.
[56] S. Itoh, K. Ozumi, H.W. Kim, O. Nakagawa, R.D. McKinney, R.J. Folz, I.N. Zelko, M. Ushio-Fukai, T. Fukai, Novel mechanism for regulation of extracellular SOD transcription and activity by copper: role of antioxidant-1, Free Radic. Biol. Med. 46 (1) (2009) 95–104, https://doi.org/10.1016/j.freeradbiomed.2008.09.039.
[57] V. Jeney, S. Itoh, M. Wendt, Q. Gradek, M. Ushio-Fukai, D.G. Harrison, T. Fukai, Role of antioxidant-1 in extracellular superoxide dismutase function and expression, Circ. Res. 96 (7) (2005) 723–729, https://doi.org/10.1161/01.RES.0000162001.57896.66.
[58] H. Gao, W. Yang, Z. Qi, L. Lu, C. Duan, C. Zhao, H. Yang, DJ-1 protects dopaminergic neurons against rotenone-induced apoptosis by enhancing ERK-dependent mitophagy, J. Mol. Biol. 423 (2) (2012) 232–248, https://doi.org/10.1016/j.jmb.2012.06.034.
[59] G.S. Kelner, M. Lee, M.E. Clark, D. Maciejewski, D. McGrath, S. Rabizadeh, T. Lyons, D. Bredesen, P. Jenner, R.A. Maki, The copper transport protein Atox1 promotes neuronal survival, J. Biol. Chem. 275 (1) (2000) 580–584, https://doi.org/10.1074/jbc.275.1.580.
[60] Q. Xue, D. Yan, X. Chen, X. Li, R. Kang, D.J. Klionsky, G. Kroemer, X. Chen, D. Tang, J. Liu, Copper-dependent autophagic degradation of GPX4 drives ferroptosis, Autophagy 19 (7) (2023) 1982–1996, https://doi.org/10.1080/15548627.2023.2165323.
[61] A. Kondo, K. Shahpasand, R. Mannix, J. Qiu, J. Moncaster, C.H. Chen, Y. Yao, Y. M. Lin, J.A. Driver, Y. Sun, et al., Antibody against early driver of neurodegeneration cis P-tau blocks brain injury and tauopathy, Nature 523 (7561) (2015) 431–436, https://doi.org/10.1038/nature14658.
[62] J. Nunnari, A. Suomalainen, Mitochondria: in sickness and in health, Cell 148 (6) (2012) 1145–1159, https://doi.org/10.1016/j.cell.2012.02.035.
[63] N. Khatri, M. Thakur, V. Pareek, S. Kumar, S. Sharma, A.K. Datusalia, Oxidative stress: major threat in traumatic brain injury, CNS Neurol. Disord.: Drug Targets 17 (9) (2018) 689–695, https://doi.org/10.2174/1871527317666180627120501.
[64] B. Belatar, A. Elabidi, M. Barkiyou, M. El Faroudi, R. Eljaoudi, L. Lahlou, S. Kabbaj, W. Maazouzi, The influence of heavy metals and trace elements on comatose patients with severe traumatic brain injury in the first week of admission, J. Toxicol. 2018 (2018) 7252606, https://doi.org/10.1155/2018/7252606.
[65] L. Mezzaroba, D.F. Alfieri, A.N. Colado Simao, E.M. Vissoci Reiche, The role of zinc, copper, manganese and iron in neurodegenerative diseases, Neurotoxicology 74 (2019) 230–241, https://doi.org/10.1016/j.neuro.2019.07.007.
[66] W. Yu, R. Parakramaweera, S. Teng, M. Gowda, Y. Sharad, S. Thakker-Varia, J. Alder, F. Sesti, Oxidation of KCNB1 potassium channels causes neurotoxicity and cognitive impairment in a mouse model of traumatic brain injury, J. Neurosci. 36 (43) (2016) 11084–11096, https://doi.org/10.1523/JNEUROSCI.2273-16.2016.
[67] M.H. Khadem-Ansari, M. Asoudeh, H.F.K. Gheshlaghi, S. Nozari, M. Zarringol, N. F. Maroufi, Y. Faridvand, Copper and zinc in stage I multiple myeloma: relation with ceruloplasmin, lipid peroxidation, and superoxide dismutase activity, Horm. Mol. Biol. Clin. Invest. 37 (3) (2018), https://doi.org/10.1515/hmbci-2018-0055.
[68] M. Yang, X. Wu, J. Hu, Y. Wang, Y. Wang, L. Zhang, W. Huang, X. Wang, N. Li, L. Liao, et al., COMMD10 inhibits HIF1alpha/CP loop to enhance ferroptosis and radiosensitivity by disrupting Cu-Fe balance in hepatocellular carcinoma, J. Hepatol. 76 (5) (2022) 1138–1150, https://doi.org/10.1016/j.jhep.2022.01.009.
[69] S. Blockhuys, X. Zhang, P. Wittung-Stafshede, Single-cell tracking demonstrates copper chaperone Atox1 to be required for breast cancer cell migration, Proc. Natl. Acad. Sci. U. S. A. 117 (4) (2020) 2014–2019, https://doi.org/10.1073/pnas.1910722117.